Gondwana Research 161 (2027) 267–284

Contents lists available at ScienceDirect

Gondwana Research

journal homepage: www.elsevier.com/locate/gr

Research paper

Seismological constraints on subduction-related tectonic evolution in the proto-Eurasian passive margin around the Korean Peninsula

Seongjun Park[1], Tae-Kyung Hong*, Jeongin Lee, Junhyung Lee, Byeongwoo Kim

Yonsei University, Department of Earth System Sciences, 50 Yonsei-ro, Seodaemun-gu Seoul 03722, South Korea

ARTICLE INFO

Keywords:
Proto-Eurasian margin evolution
Shear-wave velocity structure
Integrated ambient-noise and Eikonal tomography
Paleo-Pacific subduction
Rotational continental separation

ABSTRACT

The eastern proto-Eurasian passive margin, currently around the southeastern Korean Peninsula, experienced complex tectonic episodes of paleo-Pacific plate subduction, mantle upwelling, plutonic intrusion, continental rifting, and rotational separation of continental fragments. These multi-stage processes imprint composite tectonic signatures in the crust and upper mantle. We construct a high-resolution, three-dimensional shear-wave velocity model extending into the upper mantle by integrating ambient-noise tomography and earthquake-based Eikonal tomography. The velocity structures reveal strong low-velocity anomalies in sediment-filled basins underlain by high-velocity plutonic bodies and substantial basement relief, indicating extensive arc-related magmatism and magma underplating in the Cretaceous. Low-velocity anomalies in the upper mantle along the western margin of the Gyeongsang basin suggest thermally modified lithosphere influenced by northwestward mantle-wedge flow linked to paleo-Pacific subduction. These characteristics together with subdued mountain topography near volcanic basins suggest lithospheric extension associated with slab retreat. Along the eastern and southern coasts, strong high-velocity anomalies in the lower crust reflect mantle uplift and lithospheric thinning related to continental rifting prior to the opening of the East Sea (Sea of Japan). Low velocity perturbations along the east coast at depths of ~50–100 km suggest elevated thermal conditions produced by asthenospheric upwelling beneath the extensional margin. The spatially variable structures suggest continental rifting through multiple processes. Seismic anisotropy provides additional constraints on the deformation history, supporting clockwise rotational deformation around a pivot located near the southwestern East Sea.

1. Introduction

The East Sea (Sea of Japan) is a key area that connects the eastern margin of the Eurasian Plate with Japanese islands (Choi et al., 2012; Hong et al., 2024; Park and Hong, 2024a) (Fig. 1). Continent-scale complex tectonic evolution including plate reorganization, subduction change and slab rollback may be associated with the region (Chough and Sohn, 2010; Choi et al., 2012; Kim et al., 2015; Park and Hong, 2024a; Celis et al., 2025). There remain unresolved issues such as deep slab geometry, remanent paleo plate (Izanagi Plate) and linkage to intraplate volcanism (Kim et al., 2015; Tang et al., 2018; Ma and Xu, 2021; Celis et al., 2025).

The East Sea developed through continental rifting in the Oligocene to mid-Miocene, which resulted in the separation of the Japanese islands from the Eurasian continent (Choi et al., 2012; Kim et al., 2018, 2022; Hong et al., 2024; Park and Hong, 2024a; J. Lee et al., 2025). The high-relief bathymetry and diamond-shaped coastline was formed from multiple tectonic processes with intermittent rifting and seafloor spreading (Kim et al., 2018; Yang et al., 2022; Celis et al., 2025). The rotational opening in the East Sea made the southwestern Japanese islands rotate clockwise, while the northeastern Japanese islands counterclockwise (Martin, 2011; Yang et al., 2022). The opening process may provide information on plate reorganization, mantle convection, and regional stress evolution (Otofuji et al., 1985; Choi et al., 2012; Yang et al., 2022). However, the structural signatures have been poorly identified (Otofuji et al., 1985, 1999; Jolivet et al., 1994; Martin, 2011; Choi et al., 2012; Yang et al., 2022).

The southeastern Korean Peninsula faces the southwestern East Sea where the rotational opening occurred (Martin, 2011; Yang et al., 2022). High seismicity is observed in the reversely reactivated rifting system (Choi et al., 2012). In addition, the rotation pole for the fan-shaped opening may be located in the southwestern margin of the East Sea. The lithospheric structures around the continental-opening pivot may provide the information on lithospheric response in

* Corresponding author.
E-mail address: tkhong@yonsei.ac.kr (T.-K. Hong).
[1] *now at* Ocean Georesources Research Department, Korea Institute of Ocean Science and Technology, Busan 49111, South Korea.

https://doi.org/10.1016/j.gr.2026.08.023
Received 15 November 2025; Received in revised form 27 April 2026; Accepted 30 August 2026
Available online 5 October 2026
1342-937X/© 2026 International Association for Gondwana Research. Published by Elsevier B.V. All rights are reserved, including those for text and data mining, AI training, and similar technologies.

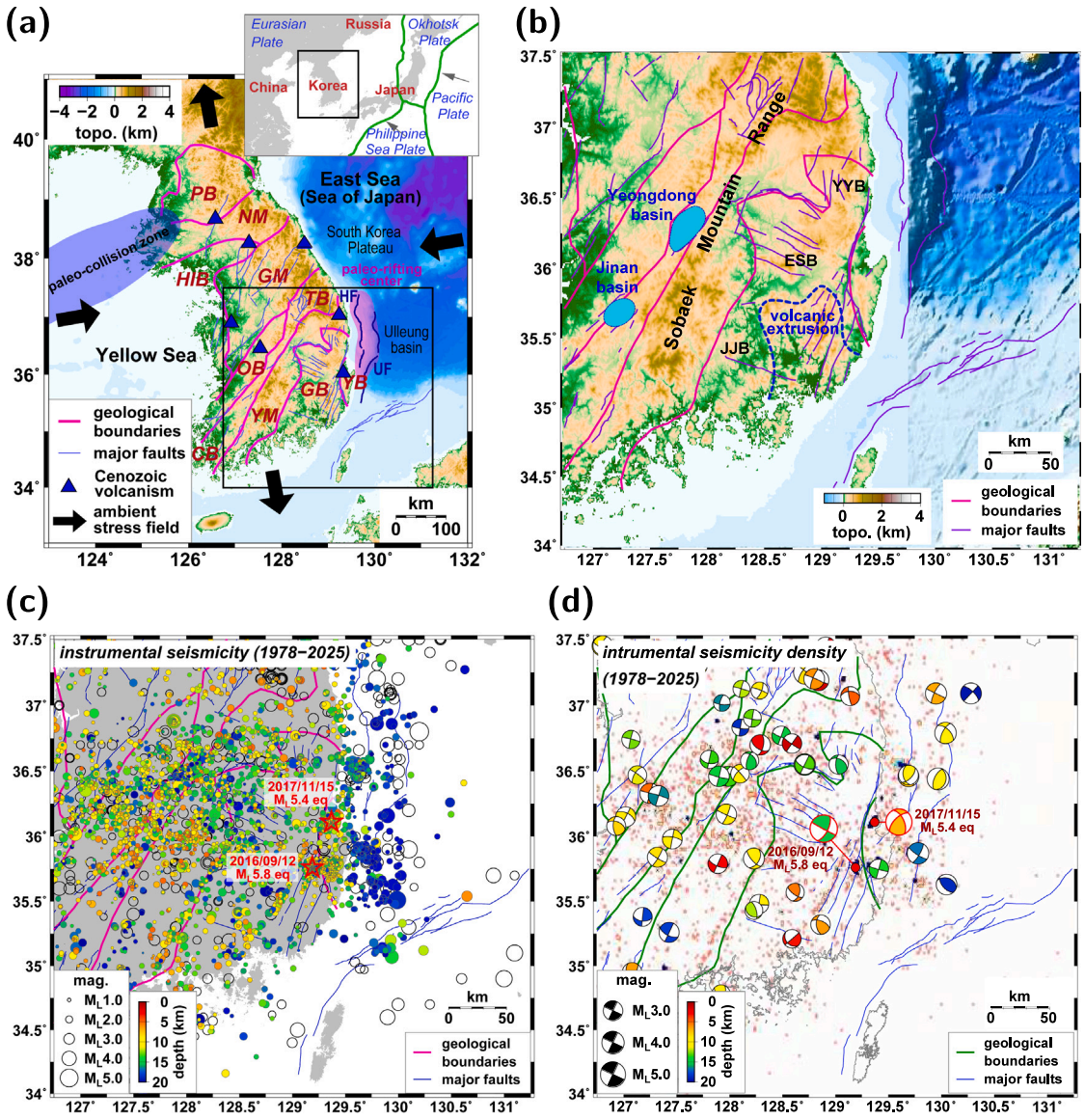

Fig. 1. (a) Geological and tectonic structures around the eastern margin of the Eurasian Plate. Major geological provinces are indicated (thick solid lines): Nangrim massif (NM), Gyeonggi massif (GM), Yeongnam massif (YM), Hongseong-Imjingang belt (HIB), Okcheon belt (OB), Pyeongnam basin (PB), Taebaeksan basin (TB), Okcheon basin (CB), Gyeongsang basin (GB), and Yeonil basin (YB). Major faults (thin solid lines) and ambient stress fields (arrows) are marked. The Ulleung fault (UF) and Hupo fault (HF) are indicated. The paleo-continental-rifting center in the western East Sea and paleo-continental-collision zone in the Yellow Sea are marked (shaded regions). The study area is indicated (box). Tectonic setting around the Korean Peninsula is presented (inset). (b) Topography map of the study region. Sobaek Mountain Range, Jinan basin, and Yeongdong basin are indicated. Subbasins in the Gyeongsang basin are indicated: Yeongyang (YYB), Euiseong (ESB), and Jinju (JJB). Volcanic-extrusion areas are marked (dotted lines). (c) Instrumental seismicity in the study region. Focal depths and magnitudes are presented. The 12 September 2016 M_L5.8 earthquake and the 15 November 2017 M_L5.4 earthquake are marked (stars). (d) Instrumental seismicity density. Focal mechanism solutions of the earthquakes are presented (Hong and Choi, 2012; Choi et al., 2012; Lee et al., 2017).

the rotational continent-opening system. The region also contains the Gyeongsang basin, a Cretaceous sedimentary basin in the southeastern Korean Peninsula. The relationship between continental rifting and the Gyeongsang basin provides constraints on the processes governing continental rift evolution. The rifting and opening of the East Sea accompany lithospheric thinning, asthenospheric upwelling, and thermal elevation, which may leave structural imprints (Choi et al., 2012; Yang et al., 2022; Park and Hong, 2024a; Celis et al., 2025; J. Lee et al., 2025).

Seismic tomography provides constraints on the lithospheric structures associated with tectonic evolution (Van van der Hilst et al., 1997; Hafkenscheid et al., 2006; Replumaz et al., 2010; Kil et al., 2021; Park and Hong, 2024a). This study investigates crust-to-upper-mantle structures around the southeastern Korean Peninsula using a combined analysis of ambient-noise tomography and earthquake-based Eikonal tomography (Park and Hong, 2024a). We examine the lithospheric and thermal structures from the seismic velocity structures, with a particular focus on identifying signatures of continental-rifting and rotational opening processes. Geological and seismological observations are integrated to constrain the tectonic evolution and rifting mechanisms in the East Sea.

2. Geological settings

The Pacific Plate and Philippine Sea Plate subduct beneath the Japanese islands that lie on the edges of the Eurasian Plate and the North American Plate. This plate subduction system generates complex stress fields and mantle flow patterns along the eastern Eurasian margin

Huang and Zhao (2006), Nakajima et al. (2006), Zhao et al. (2012), Lee et al. (2017), S. Lee et al. (2025). Mantle dynamics of the overlying big mantle wedge modulates the regional tectonics (Lei and Zhao, 2005; Zhao et al., 2007, 2009; Ma and Xu, 2021). The region has experienced complex tectonic episodes including continental collision (Hong and Choi, 2012; Hong et al., 2016; Celis et al., 2025; Hong et al., 2025; Liu et al., 2026), plate subduction (Chough et al., 2000; Kim et al., 2015; Celis et al., 2025), and continental rifting (Choi et al., 2012; Kim et al., 2018, 2022; Park and Hong, 2024a; Hong et al., 2024).

The southeastern Korean Peninsula consists of complex geological units, including two Precambrian massifs (Gyeonggi and Yeongnam massifs), a metamorphic fold-thrust belt (Okcheon belt) with Neoproterozoic and Paleozoic metasedimentary basins (Okcheon and Taebaeksan basins), and Cretaceous and Cenozoic sedimentary basins (Gyeongsang and Yeonil basins) (Fig. 1) (supplementary materials).

The East Sea is located in a back-arc region between the Eurasian continent and the Japanese islands. The East Sea was formed by the continental rifting during the Oligocene to mid-Miocene (Choi et al., 2012; Kim et al., 2022; Hong et al., 2024) (Fig. 1). Multiple rifting episodes occurred at distinct centers, forming major deep-sea basins including the Ulleung, Japan, and Yamato basins (Choi et al., 2012; Kim et al., 2018, 2022; Hong et al., 2024). The southwestern East Sea was a principal locus of the rifting with sequential east–west continental extension and breakup from north to south (Kim et al., 2018; Yang et al., 2022; J. Lee et al., 2025).

Systematic mantle uplift, asthenospheric upwelling, magma underplating, seafloor spreading occurred during the tectonic evolution (Hirata et al., 1992; Choi et al., 2012; Yang et al., 2022; Hong et al., 2024; Park and Hong, 2024a; J. Lee et al., 2025). Then, clockwise rotation of the southwestern Japanese islands relative to the Korean Peninsula led to the formation of wedge-shaped southwestern margin, fostering fan-shaped rotational opening of the southwestern East Sea (Kim et al., 2022; Yang et al., 2022; J. Lee et al., 2025). Paleomagnetic data suggest ~50–60° clockwise rotation of the southern Japanese islands with respect to the southern Korean Peninsula (Otofuji et al., 1985, 1999; Hayashida et al., 1991; Yang et al., 2022). Rotational continent opening may be driven by trench-perpendicular mantle flow (Long and van der Hilst, 2005; Lü et al., 2019; Yang et al., 2022; Celis et al., 2025).

The southeastern Korean Peninsula and the southwestern Japanese islands experienced arc-related volcanism associated with the subduction of the paleo-Pacific plate, resulting in widespread volcano-sedimentary sequences (Chough and Sohn, 2010; Kim et al., 2012; Y.I. Lee et al., 2023; S.H. Lee et al., 2023). The Gyeongsang basin, characterized by ~150–200 km-wide volcano-sedimentary strata largely occupying the southeastern peninsula, is interpreted as a back-arc basin formed during paleo-subduction (Okada, 2000; Chough and Sohn, 2010). The basin is subdivided into distinct subbasins (Euiseong, Yeongyang, and Jinju subbasins) (Chough and Sohn, 2010) (Fig. 1).

The crustal thickness decreases eastward from ~36 km in the Yeongnam massif to ~28 km near the coast, consistent with the transition from continental to oceanic crust. High surface heat flow up to ~100 mW/m^2 appears in the eastern Gyeongsang basin (Fig. 2(a), (b)). Positive Bouguer gravity anomalies of >~20 mGal are pronounced in the Gyeongsang basin, suggesting a high-density basement or uplifted structures (Ryu et al., 2006; Kim et al., 2017) (Fig. 2(c)). The crustally guided shear-wave attenuation ($Lg\ Q_0^{-1}$) reaches up to ~0.003 in the Gyeongsang and Yeonil basins, likely due to thick sedimentary layers (Hong, 2010) (Fig. 2(d)). Similarly, the crustal *P*-wave is amplified in basin areas (Fig. 2(e)).

Coast-parallel high *Pn* velocities up to ~8.2 km/s are observed along the western East Sea in both the local and regional tomography models, which is related to solidified underplated magma formed by the paleo-rifting (Choi et al., 2012; Du et al., 2022) (Fig. 2(f)). Comparable high *Pn* velocities are also present around the western Gyeongsang basin, indicating locally perturbed upper-mantle medium. The upper-crustal shear-wave velocities are distinctly low in the Gyeongsang and Yeonil basins, consistent with thick sedimentary layers (Fig. 2(g)). Similarly, the shear-wave velocities in the uppermost 30 m, V_{S30}, appear low in the Yeonil basin (Fig. 2(h)). High crustal V_P/V_S ratios up to ~1.78 appear along the east coast, which may be associated with mafic magma intrusion accompanied by the paleo-rifting (Fig. 2(i)) (Jo and Hong, 2013; Song et al., 2020; Park and Hong, 2024a).

The ambient stress field is composed of ENE-WSW compression and NNW-SSE tension (Fig. 1). The southeastern Korean Peninsula presents relatively high seismicity with M4-5 earthquakes (Hong et al., 2017, 2018; Park et al., 2021; Hong et al., 2022). The seismicity is dominated by strike-slip events with focal depths of ~5–20 km. The southwestern East Sea presents high seismicity with reverse-faulting and strike-slip events (Fig. 1(c), (d)) (Choi et al., 2012; Hong et al., 2024). The high seismicity is largely attributed to the seismic reactivation of the paleo-tectonic structures (Choi et al., 2012; Hong et al., 2024).

3. Data

Seismic networks of permanent and temporary stations are densely deployed in the Korean Peninsula (Fig. 3). We collect continuous seismic records from 476 permanent stations from the Korea Meteorological Administration (KMA), Korea Institute of Geoscience and Mineral Resources (KIGAM), Korea Hydro and Nuclear Power (KHNP), Korea Electric Power Corporation (KEPCO), Korea Water Resources Corporation (K-water), and the Yonsei Earth Observatory. Also, we obtain seismic records from 388 temporary stations. The total number of stations is 864. The stations are equipped with three-component broadband seismometers, short-period sensors, and accelerometers. The sampling rates differ by network, ranging from 20 to 200 Hz.

We analyze continuous vertical-component records for the ambient-noise tomography. We use continuous records of 526 stations in the southeastern Korean Peninsula for a two-year-long period from January 2022 to December 2023. The interstation distances are < 20 km in inland regions, which are shortest in Gyeongju area (~3 km) (Heo et al., 2024) (Fig. 3) (supplementary materials).

Also, for the earthquake-based Eikonal tomography, we analyze vertical seismic records for 468 earthquakes with magnitudes of M_W 5.5–7.9 and focal depths of < 150 km in epicentral distances of < 90° in 2022–2023. We collect 270129 vertical waveforms in total, presenting prominent Rayleigh wavetrains (Fig. 3). The earthquake information is collected from the International Seismological Centre (ISC). These events present wide azimuthal coverage over the Korean Peninsula.

4. Method

Ambient noise is dominated by high-frequency energy originating from anthropogenic, oceanic, and atmospheric processes (Hong et al., 2020; Park and Hong, 2020; Park et al., 2022; Park and Hong, 2024b, 2026). On the other hand, earthquake-generated seismic waves are rich at relatively low frequencies (Park and Hong, 2024a,b). A combined analysis of ambient-noise tomography and earthquake-based tomography may provide wide-frequency imaging to constrain the crust-to-upper-mantle structures (Park and Hong, 2024a).

The ambient-noise tomography analysis is based on interstation ambient-noise crosscorrelation function that yields the Green's function along the path between the stations (Shapiro and Campillo, 2004; Shapiro et al., 2005; Bensen et al., 2007; Yang et al., 2007; Lin et al., 2013; Kil et al., 2021; Park and Hong, 2024a). The crosscorrelation function is given by Lin et al. (2013), Goutorbe et al. (2015), Kil et al. (2021), Park and Hong (2024a),

$$C_{ij}(t) = \frac{\int u_i(t+\tau)u_j(\tau)d\tau}{\sqrt{\int \left[u_i(t+\tau)\right]^2 d\tau}\sqrt{\int \left[u_j(\tau)\right]^2 d\tau}}, \quad (1)$$

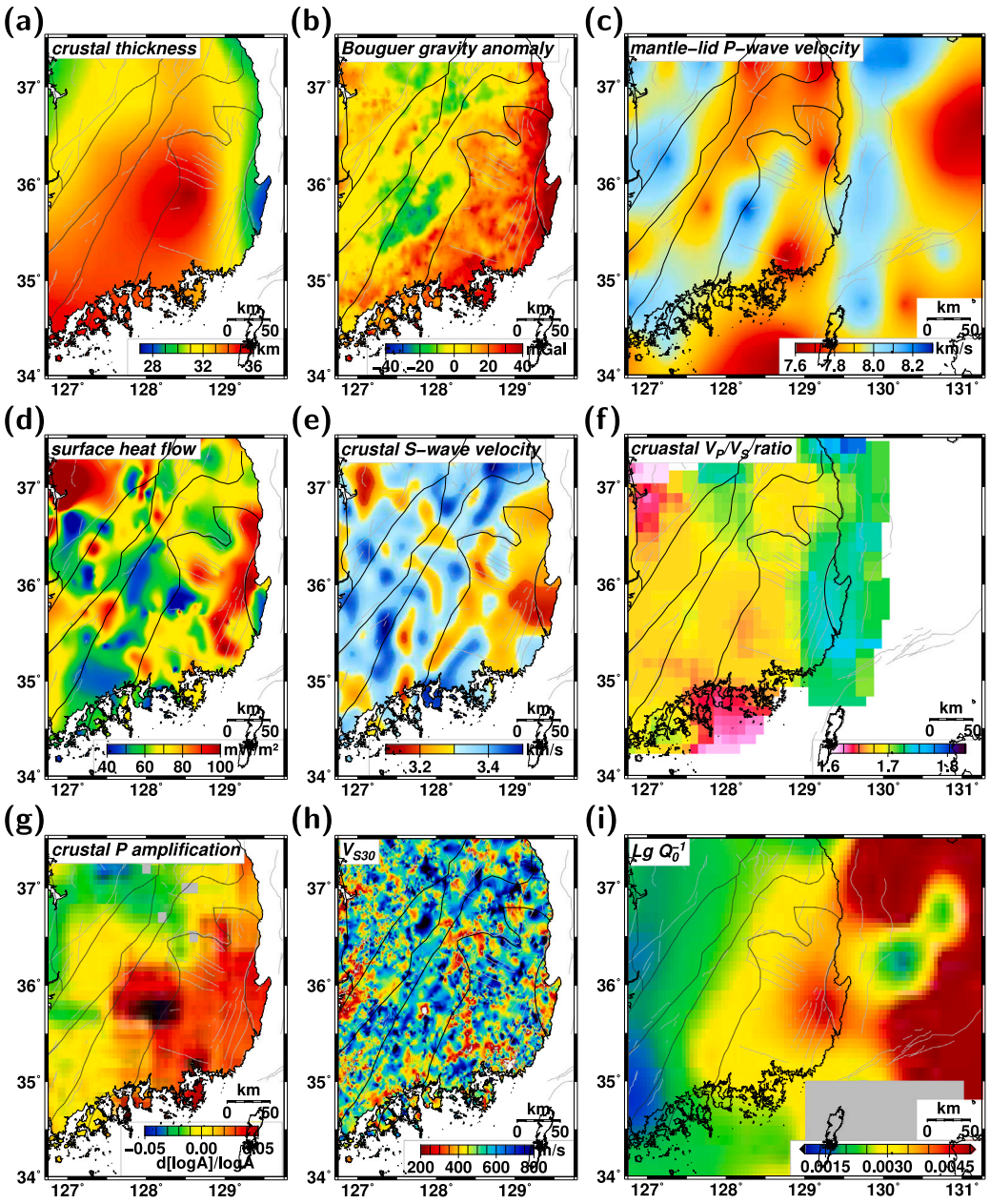

Fig. 2. Lateral variations in geophysical and seismic properties: (a) crustal thickness (Hong et al., 2008), (b) Bouguer gravity anomaly (Cho et al., 1997; Choi et al., 2021a,b, 2022), (c) mantle-lid *P*-wave velocity (Hong and Kang, 2009), (d) surface heat flow (Lee et al., 2010), (e) *S*-wave velocity at a depth of 6.75 km (Choi et al., 2009), (f) V_P/V_S ratio (Jo and Hong, 2013), (g) crustal *P* amplification (Hong and Lee, 2012), (h) average *S*-wave velocity up to a depth of 30 m (V_{S30}) (Kim and Hong, 2022), and (i) crustally-guided shear-wave attenuation ($Lg\ Q_0^{-1}$) (Hong, 2010). Geological boundaries (thick solid lines) and major faults (thin solid lines) are denoted.

where t is the delay time, C_{ij} is the waveform crosscorrelation function between stations i and j, and $u_i(\tau)$ and $u_j(\tau)$ are the waveform records at stations i and j for time τ.

The retrieved Green's function is generally dominated by fundamental-mode Rayleigh waves (Bensen et al., 2007; Kil et al., 2021; Park et al., 2021). We measure the traveltimes of Rayleigh waves using a multiple filter technique with a Gaussian filter that is given by Bensen et al. (2007), Cho et al. (2007), Goutorbe et al. (2015), Kil et al. (2021),

$$H(f) = \exp\left[-\alpha\left(\frac{f-f_0}{f_0}\right)^2\right], \quad (2)$$

where $H(f)$ is the Gaussian filter for frequency f and α is the filter-width parameter. Parameter α is scaled to the interstation distance, controlling the compromise between time and frequency resolution in the analysis (Levshin et al., 1989; Bensen et al., 2007; Kil et al., 2021; Park and Hong, 2024a).

The tomographic inversion of Rayleigh-wave group velocities determines a velocity model m to minimize the objective function $R(\mathbf{m})$,

$$R(\mathbf{m}) = \left[\mathbf{p}(\mathbf{m})-\mathbf{d}\right]^T \mathbf{C}_d^{-1}\left[\mathbf{p}(\mathbf{m})-\mathbf{d}\right] + \epsilon\left[\mathbf{m}-\mathbf{m_0}\right]^T \mathbf{C}_m^{-1}\left[\mathbf{m}-\mathbf{m_0}\right] + \eta\mathbf{m}^T\mathbf{D}^T\mathbf{D}\mathbf{m}, \quad (3)$$

where $\mathbf{p}(\mathbf{m})$ is the theoretical traveltimes for model $\mathbf{m}$, $\mathbf{d}$ is the observed traveltimes, $\mathbf{m_0}$ is the reference model, $\mathbf{C}_d$ is the data covariance matrix, $\mathbf{C}_m$ is the model covariance matrix, ϵ is the damping parameter, η is the smoothing parameter, and $\mathbf{D}$ is the second derivative operator (Rawlinson and Sambridge, 2003; Goutorbe et al., 2015; Kil et al., 2021; Park and Hong, 2024a). The inversion parameters (ϵ, η) control the tradeoff between the traveltime misfit, model roughness, and model

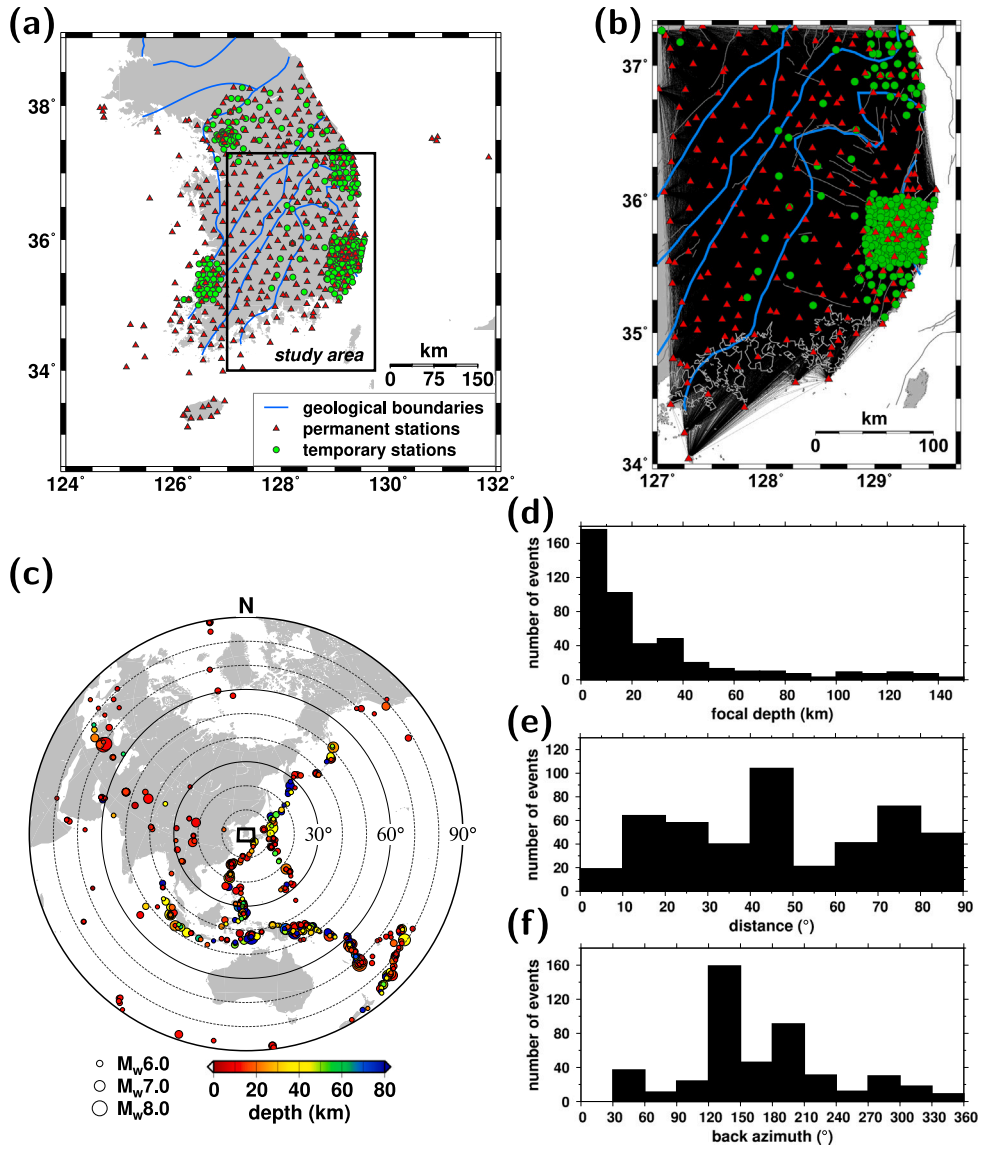

Fig. 3. (a) Seismic stations in the Korean Peninsula. The seismic stations are densely deployed in the study region (box). (b) Enlarged map of seismic stations. Interstation raypaths are presented (solid lines). (c) Locations of earthquakes for Eikonal tomography analysis. Focal depths and magnitudes of the earthquakes are indicated. Histograms for (d) focal depths, (e) epicentral distances and (f) back azimuths of earthquakes are presented. The events are distributed in wide backazimuths. The focal depths are less than 150 km, mostly less than 40 km.

variance. The parameters are determined through a sensitivity analysis (Kil et al., 2021; Park and Hong, 2024a).

We conduct Rayleigh-wave phase-velocity tomography analysis using the Eikonal method based on earthquake records (Lin and Ritzwoller, 2011b; Jin and Gaherty, 2015; Kang et al., 2016; Hao et al., 2021; Park and Hong, 2024a; Park et al., 2024). We measure the relative arrival times of Rayleigh waves at stations using a waveform crosscorrelation technique (Park and Hong, 2024a). The apparent phase velocity of Rayleigh waves is determined from the Eikonal equation (Lin and Ritzwoller, 2011a; Jin and Gaherty, 2015; Park and Hong, 2024a),

$$\frac{1}{\left|c'\left(\vec{\mathbf{r}}\right)\right|^2} = \left|\nabla T\left(\vec{\mathbf{r}}\right)\right|^2, \tag{4}$$

where $c'\left(\vec{\mathbf{r}}\right)$ is the apparent Rayleigh-wave phase velocity at location $\vec{\mathbf{r}}$, and $T\left(\vec{\mathbf{r}}\right)$ is the Rayleigh-wave traveltime at location $\vec{\mathbf{r}}$. The apparent phase velocities are affected by scattering, anisotropy, and multipath effects, exhibiting earthquake-dependent variations and spurious artifacts (Lehujeur and Chevrot, 2020). In practice, a representative phase velocity model is determined by stacking the apparent phase velocity models over earthquakes (Jin and Gaherty, 2015; Lehujeur and Chevrot, 2020; Hao et al., 2021; Park and Hong, 2024a).

5. Process

The study region (34.0°N-37.5°N, 127.0°E-129.625°E) is divided into 0.1°-by-0.125° cells. Seismic records are converted to displacement waveforms after correction for instrument responses. Also, the records are downsampled to 20 Hz. We calculate the ambient-noise crosscorrelation function every 2-hour-long record segment. The crosscorrelation functions are stacked over all segments to determine the representative Green's functions. We apply time-domain normalization and spectral whitening to suppress transient high energy and equalize spectral amplitudes. The Green's functions present prominent fundamental-mode Rayleigh wave energy with apparent group velocities around 3 km/s (Fig. 4).

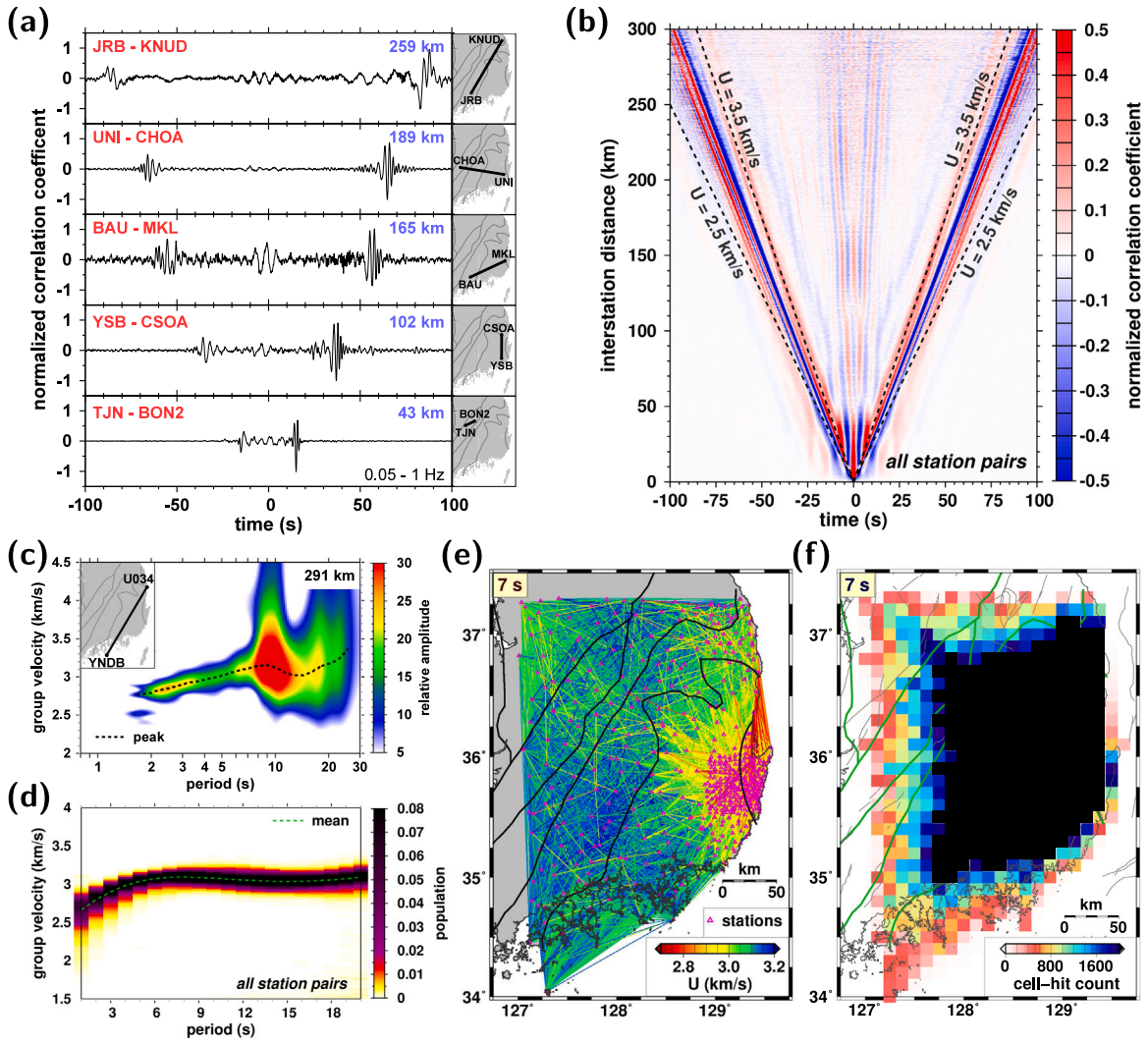

Fig. 4. (a) Examples of Green's functions retrieved from interstation ambient-noise crosscorrelation analysis. The station pairs and interstation distances are indicated. Prominent Rayleigh waves are observed. The station locations and interstation raypaths are indicated on the maps. (b) Collective Green's functions with increasing interstation distances. Robust Rayleigh wave energy appears in distances over 300 km. Theoretical Rayleigh-wave traveltime curves for group velocities (U) of 2.5 km/s and 3.5 km/s are marked (dotted lines). The dominant energy exhibits group velocities around 3 km/s. (c) Example of Rayleigh-wave dispersion analysis for station pair YNDB-U034. The station locations and interstation raypath are indicated on the map (inset). The Rayleigh-wave group-velocity dispersion curve is marked (dotted line). (d) Collective Rayleigh-wave group-velocity dispersion curves for all station pairs. The average group velocities are indicated (dotted line). (e) Raypath-dependent Rayleigh-wave group velocities at a period of 7 s, and (f) cell-hit counts at a period of 7 s. The group velocities vary by region. The group velocities vary regionally, and the raypaths densely cover the study area.

We measure the fundamental-mode Rayleigh-wave group velocities at 1–20 s from the Green's functions using the multiple filter technique (Fig. 4). We analyze the Green's functions with signal-to-noise ratios of > 3 and interstation distances of > 3 wavelengths. We set the bandwidth parameter (α) to be 3–25 that is scaled with interstation distance. We measure the group velocities from fold-averaged Green's functions for stable measurement. We only assess the group velocities when the differences of individual estimates between causal and acausal components are less than 5% (Park and Hong, 2024a). We finally obtain the group-velocity measurements for 11829–95268 raypaths depending on the frequency. Raypath coverage is high in most regions, with cell-hit counts of > 200 (Figs. 3, 4(d)). We apply the smoothing parameter of 50 and damping parameter of 200–500 (see, supplementary materials).

For Eikonal tomography, we prepare the earthquake waveform records that are Gaussian-filtered for periods of 20–80 s. We collect Rayleigh wavetrains using time windows with length of 8 periods around the peak Rayleigh-wave amplitudes. We analyze the Rayleigh waveforms with signal-to-noise ratios of > 5. We measure the interstation phase delay times using waveform crosscorrelations. Only the estimates with correlation coefficients of > 0.9 are analyzed (Park and Hong, 2024a). The phase arrival times at stations are reconstructed from these interstation delays (Park and Hong, 2024a) (Fig. 5). The phase velocities are estimated using the Eikonal equation (Jin and Gaherty, 2015; Hao et al., 2021; Park and Hong, 2024a) (Fig. 5).

Rayleigh-wave dispersion curves at periods of 1–80 s are constructed from group and phase velocities (Figs. 6, 7). We derive the shear-wave velocity models from the dispersion curves using a linearized iterative inversion method (Herrmann and Ammon, 2004). Layered velocity models down to a depth of 200 km are inverted. The *P*-wave velocities and densities are determined from the inverted *S*-wave velocities using empirical relationships (Nafe and Drake, 1963; Brocher, 2005). Considering the depth sensitivity of Rayleigh-wave

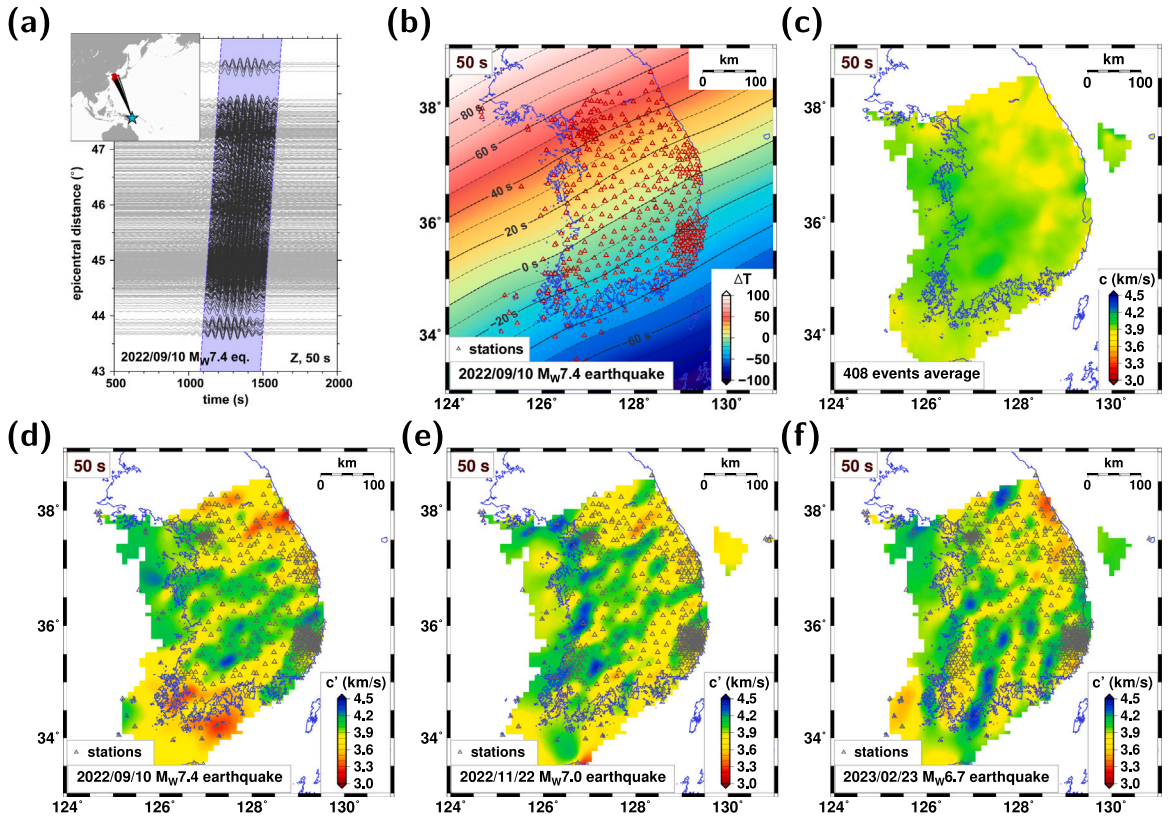

Fig. 5. (a) Vertical seismic records for the 10 September 2022 M_W 7.4 earthquake. A Gaussian filter at a period of 50 s is applied. Time windows for the Rayleigh wave analysis are indicated (shaded). Map of earthquake (star), stations (circles), and raypaths (solid lines) is presented (inset). (b) Differential traveltimes (ΔT) of Rayleigh waves at period of 50 s. The station locations are marked (triangles). Planar wavefronts with local undulations are observed. (c) Map of average Rayleigh-wave phase velocities at period of 50 s is presented. The average phase velocities smoothly change over the region with minimized event-dependent artifacts. Maps of apparent Rayleigh-wave phase velocities (c') at period of 50 s for (d) the 10 September 2022 M_W 7.4 Papua New Guinea earthquake, (e) the 22 November 2022 M_W 7.0 Solomon Islands earthquake, and (f) the 23 February 2023 M_W 6.7 Tajikistan earthquake. The apparent phase velocities present local variations.

dispersion curves, the layer thickness is set to increase with depth, from ~1 km near the surface to ~50 km at depths greater than 100 km. Consequently, the vertical resolution of the model varies with depth.

6. Validation test

We verify the tomography analyses using synthetic recovery tests (Cho et al., 2007; Hong and Kang, 2009; Jia and Clayton, 2021; Kil et al., 2021). We consider Rayleigh-wave group-velocity perturbations of ±10% in checkerboard pattern with checker sizes of 0.3°-by-0.38°, 0.4°-by-0.5°, and 0.6°-by-0.75° in the ambient-noise tomography analysis (see, supplementary materials). We produce synthetic traveltimes with random Gaussian errors of standard deviations 0.5–1.7 s. We invert velocity models from the synthetic data (see, supplementary materials). The checkerboard patterns with checker sizes down to 0.4°-by-0.5° (equivalently, lateral resolution of approximately 44 km-by-45 km) are well recovered at periods of 1–20 s. In particular, smaller perturbations of 0.3°-by-0.38° are reasonably recovered in periods ≤ 15 s, suggesting higher spatial resolution for shallow depths (supplementary materials).

For the validation test of earthquake-based Eikonal tomography analysis, we consider Rayleigh-wave phase-velocity perturbations of 10% with checker sizes of 0.4°-by-0.5° and 0.6°-by-0.75°. We add random Gaussian errors with standard deviations of 0.07–0.21 km/s to the theoretical traveltimes. The checker size of 0.6°-by-0.75° (equivalently, spatial resolution of approximately 66 km-by-67 km) is reasonably resolved in periods of 20 s to 80 s. The inversion at shorter periods of ≤ 40 s recovers the 0.4°-by-0.50° checkers, suggesting higher spatial resolution of approximately 0.44 km-by-0.45 km.

We also examine the stability of 3-D shear-wave velocity inversion (supplementary materials). We consider a synthetic shear-wave velocity model based on a checkerboard pattern with a checker size of 0.6°-by-0.75° and velocity perturbations of ±10% relative to a reference one-dimensional model. To assess the vertical resolution of the inversion, we introduce depth-dependent perturbations in which the sign of the velocity perturbation alternates at depths of 10 km, 30 km, 60 km, and 100 km (supplementary materials). Synthetic Rayleigh-wave traveltime data are generated for the synthetic input velocity model, incorporating random Gaussian errors. We sequentially perform Rayleigh-wave group-velocity inversion, Rayleigh-wave phase-velocity inversion, and shear-wave velocity inversion using the synthetic data. The lateral and vertical shear-wave velocity perturbations are well recovered up to 200 km depth at most regions.

7. Shear-wave velocity model inversion

Rayleigh waves at periods of 1–80 s are sensitive to the shear-wave velocities at depths of 0–200 km (Fig. 7). We invert the Rayleigh-wave group-velocity models at periods of 1–20 s and phase-velocity models at periods of 20–80 s (Fig. 6) (supplementary materials). The average Rayleigh-wave group velocities increase from ~2.69 km/s to ~3.10 km/s at periods 1 s to 8 s. The velocities are ~3.03 km/s at periods of 9–15 s, and reach ~3.09 km/s at the period of 20 s. The average phase velocities increase gradually from ~3.62 km/s to ~4.03 km/s

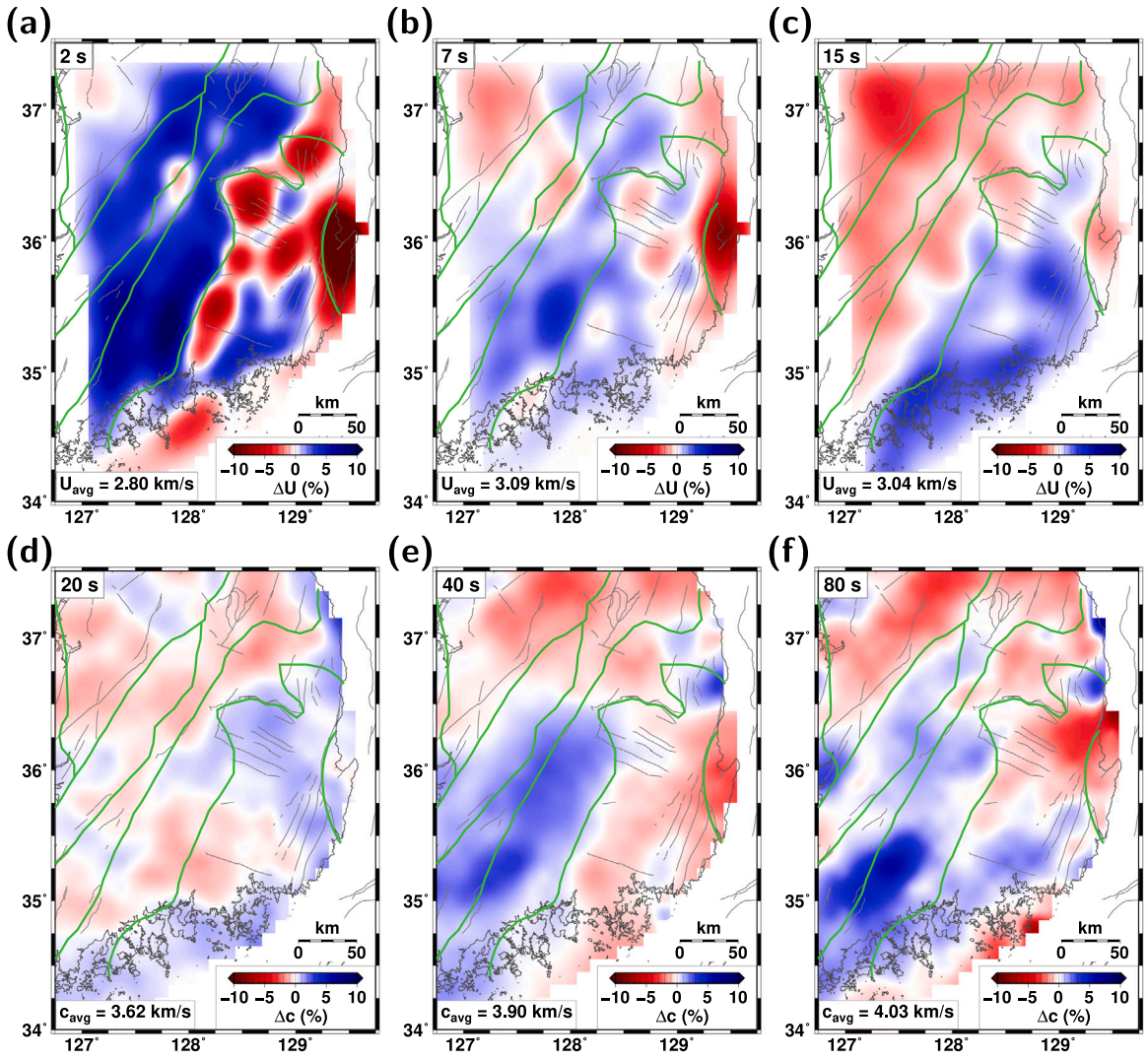

Fig. 6. Ambient-noise Rayleigh-wave group-velocity tomography at periods of (a) 2 s, (b) 7 s, and (c) 15 s, together with earthquake-based Rayleigh-wave phase-velocity tomography at periods of (d) 20 s, (e) 40 s, and (f) 80 s. Velocity perturbations (ΔU, Δc) relative to the average velocities (U_{avg}, c_{avg}) are presented. Geological boundaries (thick solid lines) and major faults (thin solid lines) are marked.

at periods of 20 s to 80 s. These period-dependent variations reflect vertical changes in the seismic velocities.

The lateral perturbations in Rayleigh-wave group velocity are as strong as -12% to 11% at the period of 1 s (Fig. 6) (supplementary materials). The perturbation strength decreases with increasing period, being -5% to 3% at the period of 20 s. The Rayleigh-wave phase velocities similarly exhibit substantial lateral perturbations exceeding ±3% over periods of 20–80 s. The lateral variations are strongly correlated with geological features. At periods of 1–6 s, the group velocities are low in Gyeongsang and Yeonil basins, and high in Yeongnam massif and Okcheon belt. The velocity perturbations are reversed at longer periods (> 6 s) with high velocities in Gyeongsang basin and low velocities elsewhere. Sharp velocity contrasts appear at periods of > 30 s along the geological boundaries between Yeongnam massif and Gyeongsang basin, distinguishing the geological properties distinctly (Fig. 6) (supplementary materials).

We invert the shear-wave velocity model from Rayleigh-wave dispersion curves using a linearized iterative inversion based on a two-step approach to update the initial models. In this approach, the updated 1-D initial model is derived from a regional average Rayleigh-wave dispersion curve, which is obtained through inversion using a previously reported 1-D model (Fig. 7). The reference model at shallow depths of <~5 km presents low velocities that may be attributed to the thick sedimentary cover in the Gyeongsang and Yeonil basins. The velocities increase abruptly at depths of ~25–35 km, which corresponds to the Moho discontinuity. The mild velocity decrease at depths of ~60–80 km forms a low-velocity zone that may correspond to the lithosphere-asthenosphere boundary (LAB) (Pasyanos et al., 2014; Lee et al., 2022; S. Lee et al., 2025). At depths greater than about 80 km, shear-wave velocities turn to increase with depth.

A one-dimensional shear-wave velocity model is determined for each grid point (see supplementary materials). We evaluate the uncertainty of the inverted models using Markov chain Monte Carlo analysis, confirming the robustness of the inversion results (see supplementary materials). The Gyeongsang and Yeonil basins present strong low velocities at shallow depths due to the sedimentary cover, and mild low velocities around the lithosphere-asthenosphere boundary. On the other hand, the Yeongnam massif presents relatively high velocities at shallow depths and mild velocity decreases in the upper mantle (Song

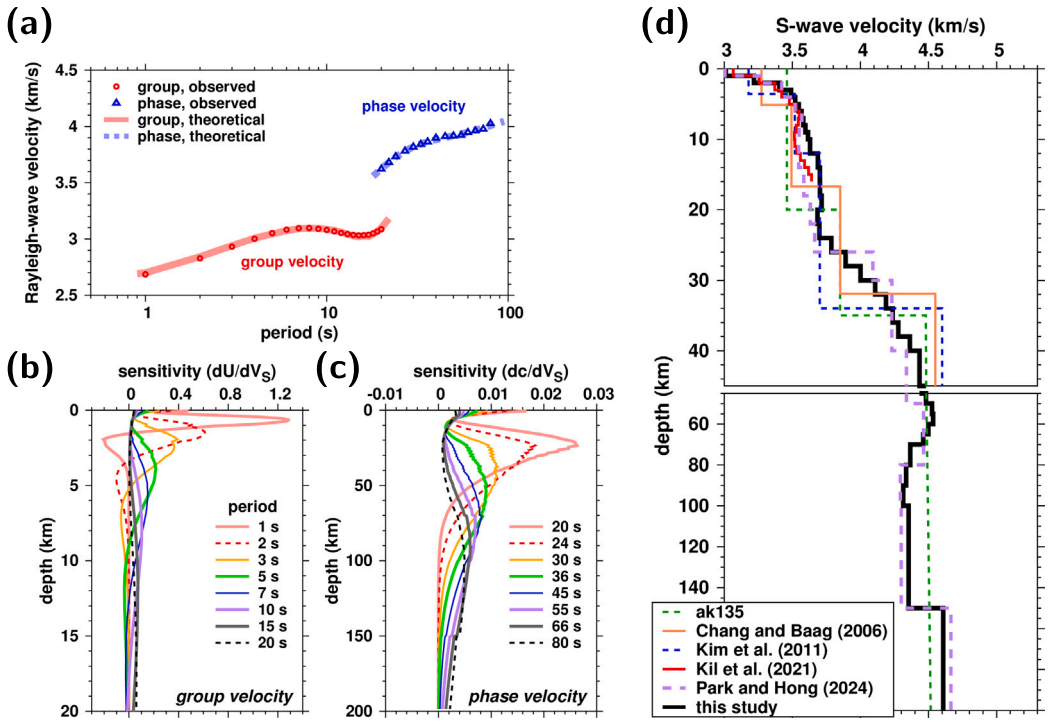

Fig. 7. (a) Reference Rayleigh-wave velocity dispersion curves for the study region. The observed dispersion curves (open symbols) are compared with the theoretical dispersion curves (solid and dotted lines), presenting good agreement at periods of 1–80 s. Sensitivity kernels of Rayleigh-wave (b) group velocities (U) and (c) phase velocities (c) as a function of depth for different periods. (d) Inverted 1-D shear-wave velocity model. *S*-wave velocity models for the global-average Earth (ak135) (Kennett et al., 1995), entire Korean Peninsula (Chang and Baag, 2006), Gyeongsang basin Kim et al. (2011), central-western Korean Peninsula (Kil et al., 2021), and central Korean Peninsula (Park and Hong, 2024a) are compared.

et al., 2020; Park and Hong, 2024a). A 3-D shear-wave velocity model is compiled from the 1-D models at grid points (Figs. 8, 9). The model is consistent with the velocity models of previous studies (Song et al., 2020; Park and Hong, 2024a) (Fig. 10(a)) (see, supplementary materials). The inverted 3-D model presents high resolution on small-scale structures.

8. Shear-wave velocity model

At shallow depths (<~ 6 km), the velocity models present strong correspondence to the surface geology. We observe pronounced low-velocity anomalies of around −7% in Gyeongsang basin (L1-L4 in Fig. 8). Notably, we observe low-velocity anomalies that align with basins (Euiseong, Yeongyang, and Jinju) (L1, L2, L3 in Fig. 8). The low velocity anomalies are distinct in Euiseong basin (L1a, L1b, and L1c in Fig. 8). On the other hand, we observe high-velocity anomalies in the southern Gyeongsang basin with extrusive volcanic rocks (H1 in Fig. 8). Similarly, Yeonil basin presents low-velocity anomalies down to around −13% (L4 in Fig. 8). The low velocities may reflect lower degrees of sediment consolidation of young strata (S. Lee et al., 2023). Also, relatively mild low-velocity anomalies of >~ −3 % appear near Yeongdong basin (L5 in Fig. 8). On the other hand, high velocities appear in Yeongnam massif, Okcheon belt, and Okcheon basin.

The low velocity anomalies at shallow depths in the basin regions diminish with increasing depth. The vertical extent of the low-velocity anomalies may suggest the thickness of sedimentary fills (Braeuer and Bauer, 2015; Hidayat et al., 2021; Cho et al., 2025). The low velocity anomalies terminate at depths of ~4 km in Yeongyang basin, ~6 km in Jinju basin, ~7 km in Euiseong basin, ~11 km in the northern Yeonil basin, and ~5 km in Yeongdong basin (L1, L2, L3, L4, L5, L6 in Fig. 8). The strong low-velocity anomalies in the northern Yeonil basin agree with high heat flows (Figs. 2, 8). Also, it is noteworthy that the observation is consistent with gravity surveys (Ryu et al., 2006).

High-velocity anomalies appear at the upper crust (depths of ~6–20 km) in Gyeongsang basin (H2 in Fig. 8). The high velocities are consistent with previous local tomography studies (Kim et al., 2017). These high-velocity anomalies are encompassed by low-velocity anomalies in surrounding regions (Yeongnam massif, Okcheon belt, Gyeonggi massif). Notably, the shear-wave velocities reach ~3.7 km/s at depths of ~10 km in Gyeongsang basin. Comparable velocities appear at depths of > 20 km in adjacent regions (H2 in Fig. 8).

We observe westward-dipping high-velocity structures at the lower crust (depths of ~20–30 km) along the east coast (H3 in Figs. 8, 9). The coast-parallel Moho uplift is consistent with receiver function studies (Chang and Baag, 2006; Hwang and Chang, 2023; J. Lee et al., 2025). The coastal high-velocity anomalies extend to the depths of ~40 km. However, the middle region around latitude of 36.5° presents a velocity transition (high-velocity anomalies to low-velocity anomalies) at depths of ~30–40 km, separating two high-velocity bodies (H3a and H3b in Fig. 8).

At depths of > 50 km, the shear-wave velocities are generally low in the eastern regions and high in the western regions (Fig. 8). We find small-scale anomalies (L7-L10, H4, and H5 in Fig. 8). We identify low-velocity anomalies with widths of ~50 km along the northern and southern coastal areas (L7 and L8 in Fig. 8). The northern low-velocity anomalies (L7 in Fig. 8) extend to the north, being connected to strong low-velocity anomalies along the east coast that are associated with mantle uplift (Park and Hong, 2024a) (Fig. 10(a)).

Notable low velocity anomalies elongated in NNE-SSW (length of ~150 km and width of ~50 km) appear at depths of ~50–150 km along the western boundary of Gyeongsang basin (L10 in Figs. 8, 9). Also, high-velocity anomalies broadly extend across the southwestern Korean Peninsula (H5 in Figs. 8, 9). We observe distinct velocity contrasts along the boundary between Gyeongsang basin and Yeongnam massif.

We also identify asthenospheric low-velocity anomalies spanning from the southern Gyeonggi massif to the southern Taebaeksan basin

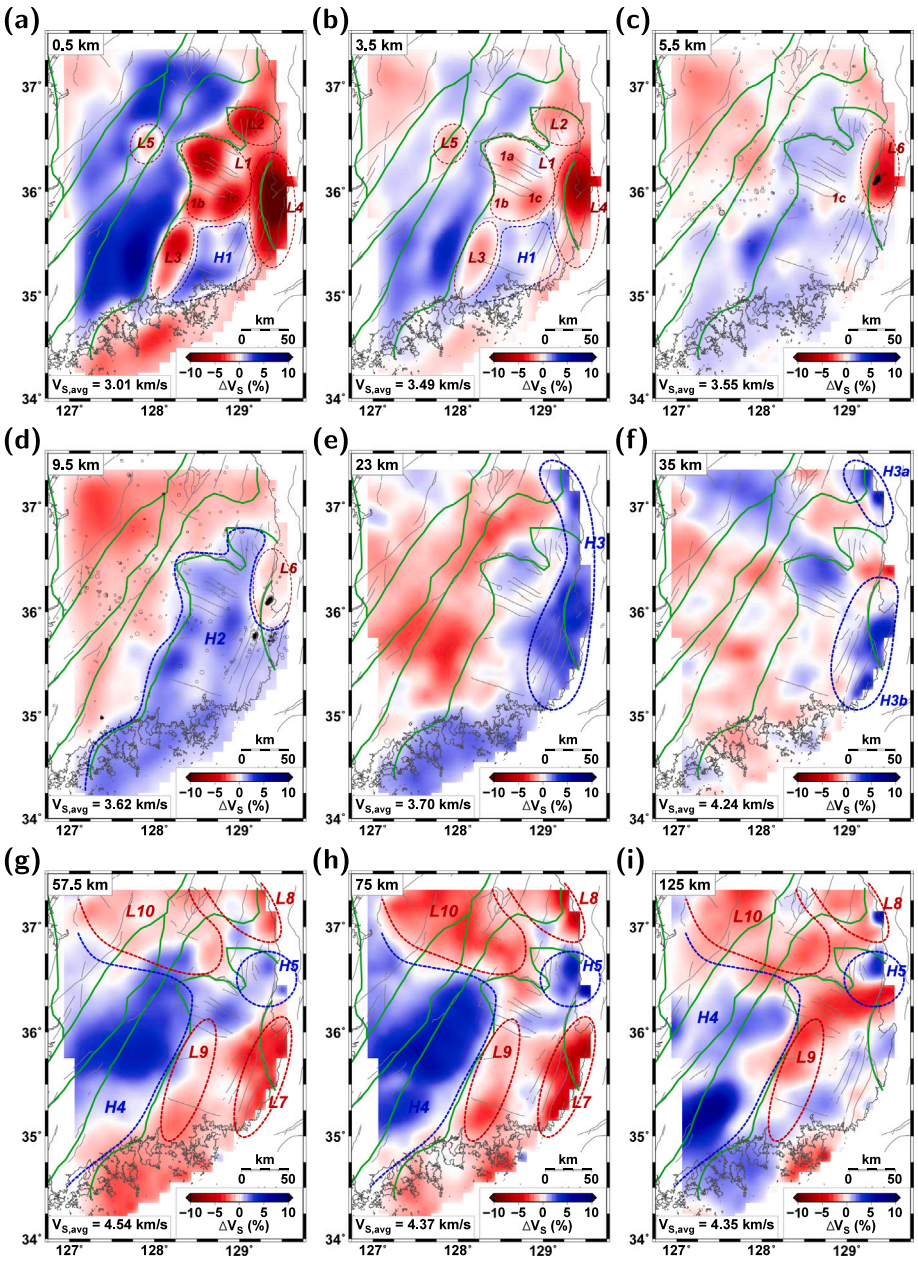

Fig. 8. Shear-wave velocity tomography at depths of (a) 0.5 km, (b) 3.5 km, (c) 5.5 km, (d) 9.5 km, (e) 23 km, (f) 35 km, (g) 58 km, (h) 75 km, and (i) 125 km. Differential velocities (ΔV_S) relative to the average velocities ($V_{S,\mathrm{avg}}$) are presented. Geological boundaries (thick solid lines) and major faults (thin solid lines) are indicated. Seismicity at corresponding depths is marked (open circles). Apparent low- and high-velocity structures are indicated (L1-L10 and H1-H5).

through the central Okcheon belt (L9 in Fig. 8). The anomalies extend northward to the low-velocity anomalies across the central to eastern Gyeonggi massif (Song et al., 2020; Park and Hong, 2024a). The low-velocity anomalies are spatially correlated with Cenozoic volcanism (Kim et al., 2015; Song et al., 2020; Kim et al., 2024).

9. Discussion

Seismic velocities reflect the combined effects of rock composition, crystal and structural orientation, temperature, and stress within the medium. We interpret the inverted seismic velocity models in conjunction with geological context, geochemical observations, and other geophysical and seismological constraints to infer lithospheric structures and tectonic evolution.

9.1. Structures and properties

Lateral variation in equi-velocity depths for 3.9–4.1 km/s may provide a first-order proxy of Moho undulation (Fig. 11) (Li et al., 2013; Park and Hong, 2024a). The depths for the velocities are the largest beneath Yeongnam massif, decreasing progressively toward the east coast. The Moho geometry broadly agrees with the receiver function studies (Chang and Baag, 2006; J. Lee et al., 2025). The mantle uplifts in the northern and southern coastal regions (> 5 km) are larger than those in the central coastal region (~2–3 km) (Figs. 11, 12). The Sobaek Mountain Range develops in a thick-crust region.

The Moho uplift is observed along the east coast (Park and Hong, 2024a). The Moho uplift may be associated with the crustal thinning and mantle upwelling during the continental rifting in the East Sea

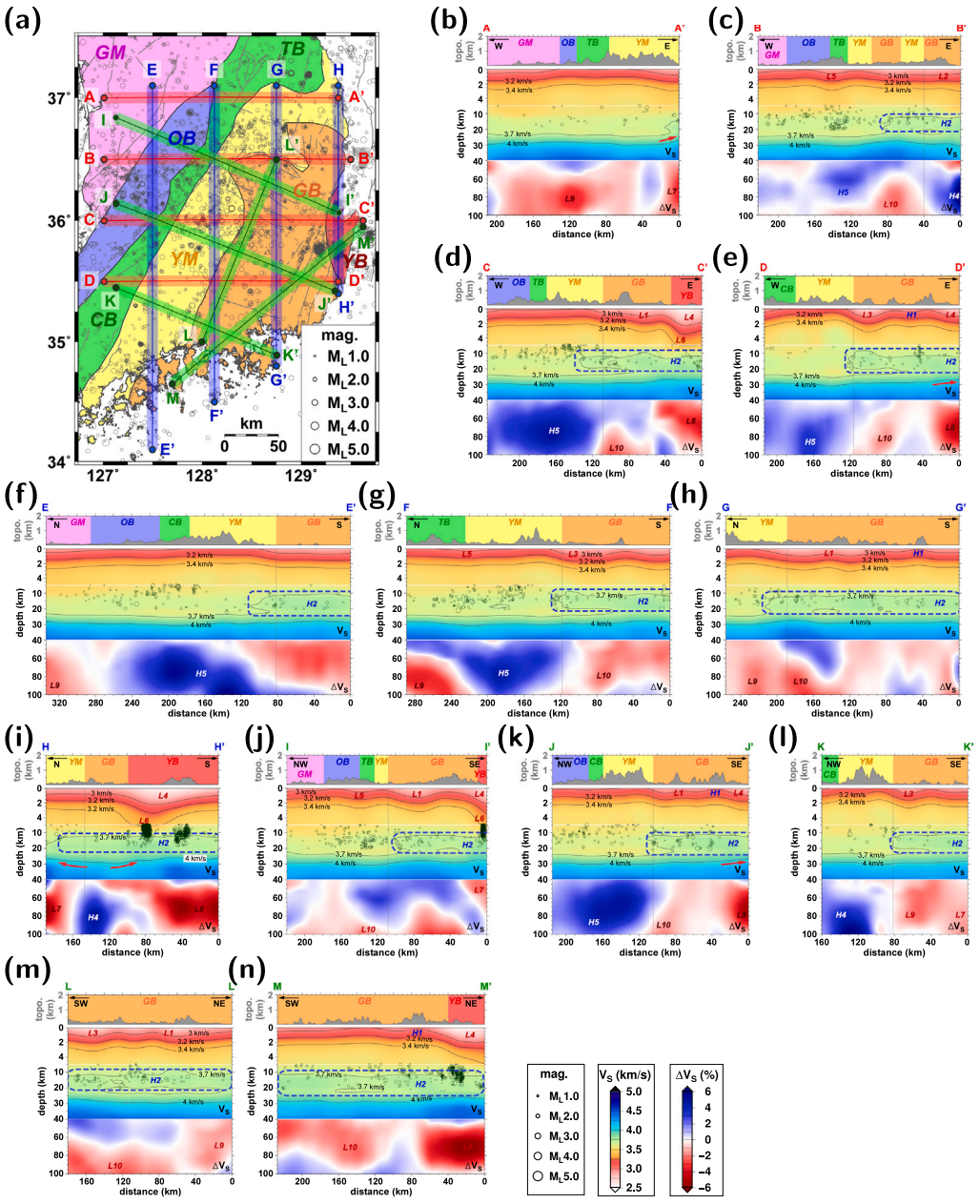

Fig. 9. Cross-sections of shear-wave velocity structures: (a) map of profiles, and shear-wave velocity models along profiles (b) AA', (c) BB', (d) CC', (e) DD', (f) EE', (g) FF', (h) GG', (i) HH', (j) II', (k) JJ', (l) KK', (m) LL', and (n) MM'. Shear-wave velocities at depths of < 50 km and differential shear-wave velocities at depths of 50–100 km are presented. The uppermost 5 km are vertically exaggerated. The seismicity is presented (open circles). The surface topography is displayed on the top. Noticeable low- and high-velocity structures are indicated (L1-L10 and H1-H5).

(Choi et al., 2012; Hong et al., 2024; Park and Hong, 2024a; J. Lee et al., 2025). We observe the coast-parallel rift structures consistently in the crust to upper mantle. We observe upper-mantle low-velocity anomalies in the northern and southern coastal regions which may be associated with mantle uplift (R1 and R2 in Fig. 12). The feature is mild in the intervening region (R3 in Fig. 12).

The upper-mantle low-velocity anomalies along the east coast may be associated with elevated temperatures related to asthenospheric upwelling, which is supported by observations of mantle gas emissions (Song et al., 2020; Kim et al., 2024; S. Lee et al., 2023) (Fig. 13). In contrast, the high-velocity anomalies in the intervening region (H4 in Fig. 8) may indicate a localized, relatively cold lithospheric fragment (Song et al., 2020; S. Lee et al., 2023) (Fig. 13). The observations are supported by positive *Pn* velocity anomalies and high crustal V_P/V_S ratios in the northern and southern regions, which may be indicative of mafic magma intrusion and magma underplating (Hong and Kang, 2009; Jo and Hong, 2013) (Fig. 12).

The lateral variations in crustal shear-wave velocities present contrasts between the western and eastern Gyeongsang basin, which is also supported by the crustal V_P/V_S ratios (Fig. 2). The V_P/V_S ratios are ~1.65–1.70 in the western area, which may be associated with felsic-to-andesitic intrusion from arc magmatism (Fig. 2) (Chough and Sohn, 2010; Y.I. Lee et al., 2023; S.H. Lee et al., 2023). On the other hand, the eastern area presents relatively high V_P/V_S ratios (~1.70–1.75), which

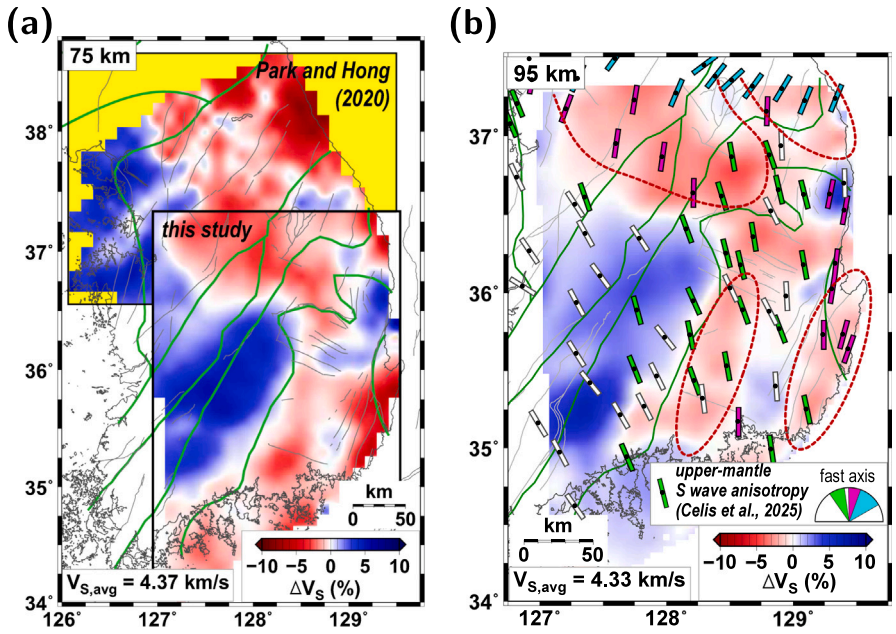

Fig. 10. (a) Comparison of shear-wave velocity models between this study and a previous study for the central-eastern Korean Peninsula (Park and Hong, 2024a). The seismic velocities for the overlapped region are matched, supporting the inversion results. (b) Comparison between shear-wave velocities at a depth of 95 km and upper-mantle fast *S*-wave orientations (Celis et al., 2025). The fast shear-wave direction varies by region.

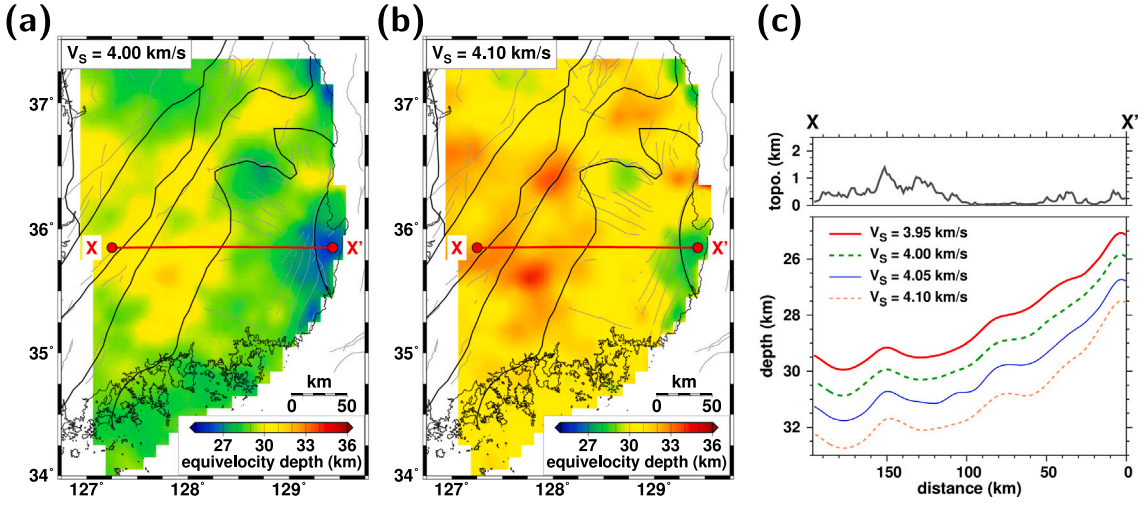

Fig. 11. Maps of equivelocity depths for shear-wave velocities of (a) 4.0 km/s and (b) 4.1 km/s. Profile XX' is indicated. The equivelocity depths are shallow along the east coast, and relatively large around the Yeongnam massif. (c) Variations of equivelocity depths for shear-wave velocities of 3.95–4.1 km/s along profile XX'. The surface topography is presented. The equivelocity depths gradually decrease to the east.

may be associated with mafic intrusion due to the continental-rifting in the East Sea (Fig. 2) (Choi et al., 2012; Yang et al., 2022; Park and Hong, 2024a; J. Lee et al., 2025).

The southwestern East Sea was formed through multi-stage rifting sequences that occurred from the north to the south (Kim et al., 2007, 2022; Celis et al., 2025). The consistent parallel geometry between the coastline, uplifted mantle, and upper-mantle low-velocity anomalies may indicate the rift-axis geometry along NW-SE direction in the northern region (R1 in Fig. 12) and N-S to NNE-SSW direction in the southern region (R3 in Fig. 12). The presence of intervening area between the northern and southern regions may suggest fragmented rift structures (R3 in Fig. 12), implying rotation of southern segment with respect to the northern segment.

The upper-mantle low-velocity anomalies along the western margin of the Gyeongsang basin spatially coincide with high *Pn* velocity anomalies (R4 in Fig. 12), which may be associated with magma underplating structures (Hong and Kang, 2009) (Fig. 13). The low-to-moderate crustal V_P/V_S ratios (~1.65–1.70) at Gyeongsang basin suggest that the mantle-derived Moho-underplated magma might rarely ascend into the crust (Fig. 12).

9.2. Tectonic implications

The southeastern Korean Peninsula experienced a series of multiple tectonic evolutions including mantle upwelling by subducting slab,

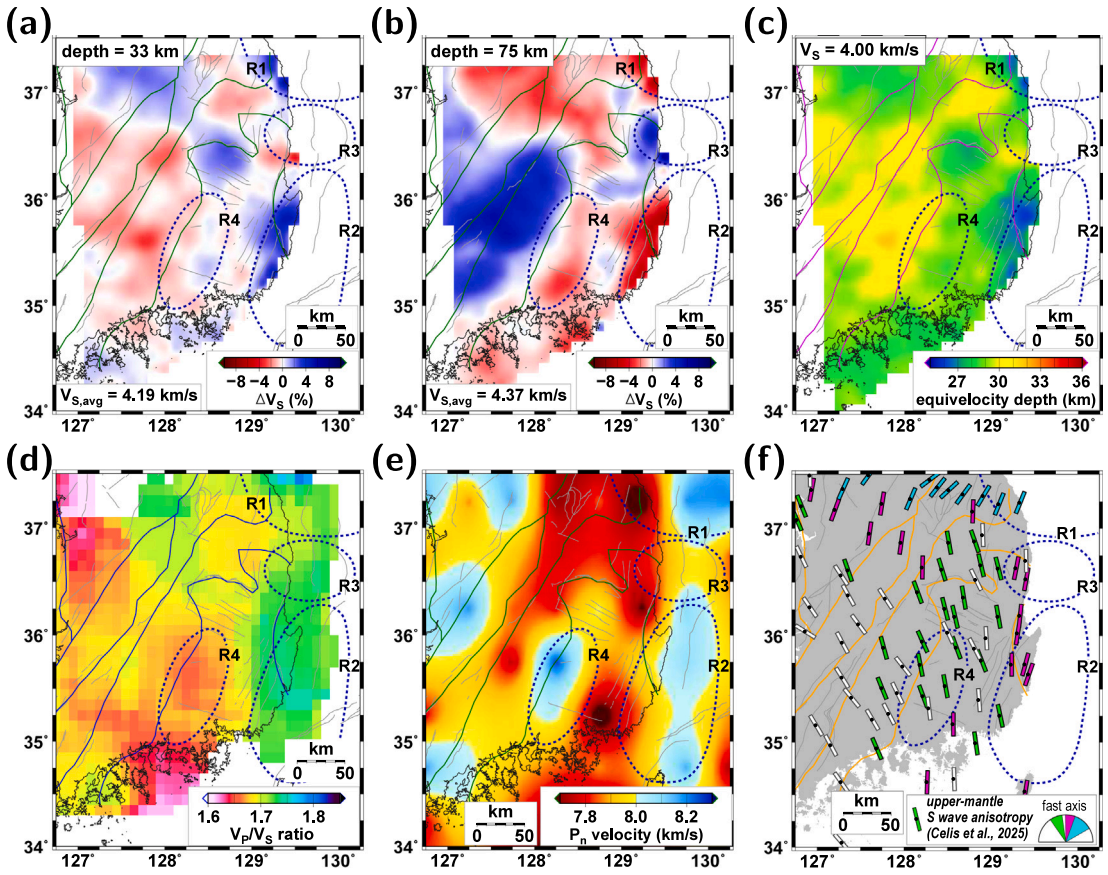

Fig. 12. Comparison among seismic properties around continental-rifting and rotational-opening regions: shear-wave velocities at depths of (a) 33 km and (b) 75 km, (c) equivelocity depths for shear-wave velocity of 4.0 km/s, (d) upper-crustal V_P/V_S ratios, (e) mantle-lid *P*-wave (*Pn*) velocities, and (f) fast shear-wave directions in the upper mantle (Celis et al., 2025). Continental-rifting signatures are pronounced along the east coast. Fragmented rift structures (R1 and R2) suggest successive episodes of continental rifting and rotational opening.

continental rifting, continental breakup, and rotational oceanic opening. Such complex tectonic evolutions are hardly distinguishable from single seismic observations. Further, these tectonic episodes are partly imprinted in the continental structures.

Before the Cretaceous, the Korean Peninsula and the proto-Japanese islands were contiguous. The paleo-Pacific plate (Izanagi Plate) subducted northwestward beneath the proto-Japanese islands and southeastern Korean Peninsula that lay along a volcanic arc (Chough and Sohn, 2010; Kim et al., 2015). The plutonic intrusions and mantle wedge flow elevated the temperature, leading to thermal weakening of lithosphere around the southeastern proto-Korean Peninsula (Syracuse et al., 2010; Kim et al., 2015; S. Lee et al., 2023). On the other hand, beneath the southwestern Korean Peninsula, we identify high-velocity anomalies in the upper mantle, which may suggest the presence of a relatively strong remnant lithospheric root (Figs. 8, 9). Further, we observe a coherent pattern of upper-mantle seismic anisotropy derived from shear-wave splitting analysis of core-refracted phases, which supports northwestward mantle flow (Celis et al., 2025) (Fig. 10(b)). These observations are consistent with the expected features of northwestward mantle-wedge flow and westward decrease in thermal modification (Song et al., 2020; Celis et al., 2025).

Such mantle dynamics may reflect a long-lived tectonic imprint associated with paleo-Pacific plate subduction, in which paleo-Pacific slab rollback may have induced WNW-ESE lithospheric stretching and asthenospheric upwelling during the early to late Cretaceous, leading to the development of the proto-Gyeongsang basin in the southeastern Korean Peninsula (Chough and Sohn, 2010; S.H. Lee et al., 2023). The extrusive rocks attest to paleo-volcanism in the Gyeongsang basin (Chough and Sohn, 2010; Y.I. Lee et al., 2023; S.H. Lee et al., 2023; Song et al., 2020). The volcanism accompanied intrusion of the magma, forming pronounced basement relief and felsic to andesitic plutons in the crust (Chough and Sohn, 2010; Y.I. Lee et al., 2023). These features may make the Gyeongsang basin be imaged distinctively as a low velocity region at shallow depths (< 4 km), while high at the lower crust (5–23 km). The observation suggests magma underplating under the Moho in the Gyeongsang basin (Figs. 8, 9). The velocity anomalies delineate the NNE-SSW-trending geometry, suggesting that the Gyeongsang basin was formed in WNW-ESE direction.

The consecutive velocity structures in the upper mantle suggest that the thermal processes during the Gyeongsang basin formation might extend to the asthenosphere (Fig. 13). Also, the upper-mantle seismic anisotropy is consistent with the lithospheric stretching direction. The seismic velocity anomalies and seismic anisotropy support the slab-rollback episode. The difference in fast shear-wave directions between the Yeongnam massif and Gyeongsang basin may suggest that the thick lithosphere of the Yeongnam massif might induce edge-driven mantle flows along the boundary (King and Anderson, 1998; Song et al., 2020; Sun and Liu, 2023; Kim et al., 2024). Also, the observations suggest basin-wide emplacement of plutons and underlying extensive paleo-magmatism (Fig. 13).

The continental rifting in the Oligocene to mid-Miocene opened the East Sea, being accompanied by asthenospheric upwelling (Kim et al.,

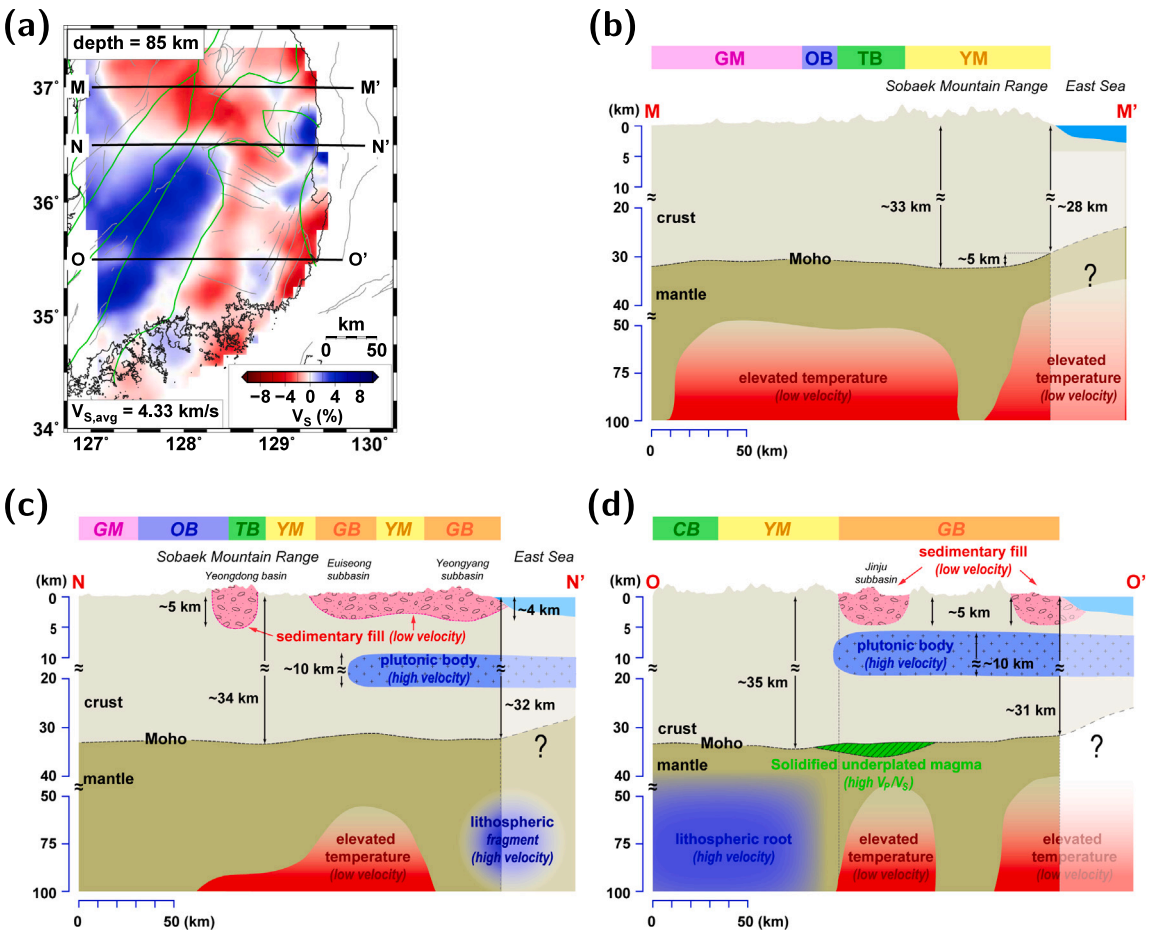

Fig. 13. Schematic model of paleotectonic structures: (a) map of shear-wave velocity profiles, and schematic models for profiles (b) MM', (c) NN', and (d) OO'. Topography along the profiles is presented. Major geological provinces are indicated: Gyeonggi massif (GM), Okcheon belt (OB), Taebaeksan basin (TB), Okcheon basin (CB), Yeongnam massif (YM), and Gyeongsang basin (GB). Sedimentary strata cover the basin areas. The crustal thicknesses are ~33–35 km beneath the Sobaek Mountain Range, decreasing eastward to ~28–32 km near the east coast. High-velocity plutonic bodies are emplaced beneath the Gyeongsang basin. At depths of > 50 km, low velocity anomalies linked to elevated temperatures are prominent.

2018, 2022). This tectonic evolution led to axis-perpendicular lithospheric thinning and stretching, potentially associated with the dynamics of the big mantle wedge (Park and Hong, 2024a; J. Lee et al., 2025; Celis et al., 2025; Lei and Zhao, 2005; Zhao et al., 2007, 2009). This geodynamic imprint is effectively preserved along the coast of the eastern Korean Peninsula. We find a decrease in crustal thickness toward the east and high-velocity anomalies along the coast at depths around 23 km, suggesting Moho uplift and continental rifting (Figs. 8, 11).

The southwestern East Sea was opened through multiple rifting episodes including east–west opening and clockwise rotation, which may be partly imprinted in the southeastern margin of the Korean Peninsula (Kim et al., 2018, 2022). We find high velocity anomalies along the east coast to the south coast at depths of 23 km (Fig. 8). Further, the fast-wave directions change along the coast, presenting NW-SE in the northern east coast, N-S in the southern east coast, and NE-SW in the south coast (Fig. 10(b)). The feature suggests that continental-side rift structures are curvilinear along the coast. These observations are consistent with regional seismic tomography models and paleomagnetic observations (Otofuji et al., 1985, 1999; Yang et al., 2022), supporting a multi-stage tectonic evolution involving continental rifting and clockwise rotation about a pole located off the south coast (Fig. 14). These sequential rifting stages, with their shifting orientations, altered the sea opening direction (Kim et al., 2018, 2022).

10. Conclusions

The eastern margin of the Eurasian Plate experienced a series of tectonic processes associated with paleo-plate subduction, mantle dynamics, and subsequent continental rifting and rotation. The lithospheric architecture and its seismic imprints have been partially constrained for the prolonged and multi-stage tectonic events. In particular, the relationships between crust-mantle deformation and sequential tectonic drivers have not been fully resolved. This study elucidates the successive tectonic episodes preserved in the present-day crustal and upper-mantle structures. We integrated ambient-noise tomography and earthquake-based Eikonal tomography, yielding a high-resolution 3-D shear-wave velocity model that presents the hereditary tectonic signatures.

The seismic observations demonstrate that the southeastern Korean Peninsula preserves a composite record of long-term tectonic evolution. The constructed shear-wave velocity model is broadly consistent with reported geological features and tectonic history. The sedimentary fills in basins are characterized by prominent low-velocity anomalies, illuminating complex basin architectures with high basement relief. High-velocity signatures characterize the volcanic edifices in the southern Gyeongsang basin. In addition, high-velocity features are identified in plutonic bodies within the mid-crust beneath the Gyeongsang basin.

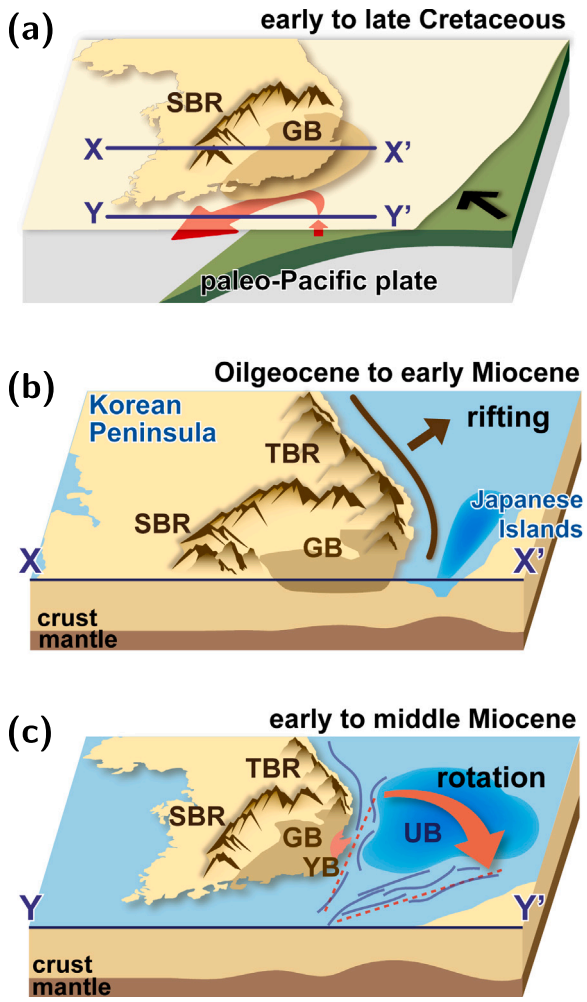

Fig. 14. Tectonic evolution model in the eastern proto-Eurasian plate with major geological structures including Sobaek Mountain Range (SBR), Taebaek Mountain Range (TBR), Gyeongsang basin (GB), Ulleung basin (UB), and Yeonil basin (YB): (a) paleo-Pacific plate subduction in the early to late Cretaceous, (b) continental rifting in the Oligocene to early Miocene, and (c) clockwise continental rotation in the early to middle Miocene. The locations of crosssection profiles (XX', YY') are marked. Gyeongsang basin is formed during the paleo-Pacific subduction. Sobaek Mountain Range develops at the northern outskirts of Gyeongsang basin. The continental rifting separates the Korean Peninsula and Japanese islands, developing Ulleung basin. The clockwise continental rotation forms the current geological setting.

In contrast, low-velocity zones occur at upper-mantle depths along the western margin of the Gyeongsang basin.

These features suggest massive arc magmatism associated with the paleo-Pacific plate subduction. High-velocity perturbations in the lower crust support magma underplating and plutonic intrusion during basin development. The observed anisotropy aligns with the extension direction, and the difference in fast-wave orientations between the Yeongnam massif and Gyeongsang basin indicates possible edge-driven mantle flow along the lithospheric thickness contrast. These observations collectively support that thermal and tectonic processes associated with Cretaceous basin formation extended from the crust into the upper mantle.

High shear-wave velocity anomalies in the upper mantle and coherent anisotropy patterns indicate the presence of a strong lithospheric root in the southwestern Korean Peninsula, consistent with pre-Cretaceous arc magmatism and northwestward mantle-wedge flow associated with subduction of the paleo-Pacific plate. These features suggest that arc-related processes preceding the Cretaceous have left a lasting imprint on the present-day lithosphere.

Subsequent continental rifting in the Oligocene to mid-Miocene produced lithospheric thinning and Moho uplift along the eastern Korean Peninsula. Notable signatures of continental-rifting in the East Sea are identified along the east coast. Westward-dipping high-velocity structures develop in the lower crust, suggesting continent-side mantle uplift. Also, strong low velocity anomalies at upper-mantle depths are attributed to the elevated temperature due to asthenospheric upwelling. The rifting signatures are pronounced locally in the northern and southern regions, suggesting multiple segmented rifting episodes (Kim et al., 2007, 2022).

The coastal high-velocity anomalies near the Moho (at ~23 km depth), together with curvilinear anisotropy patterns, reflect multi-stage rifting involving both NW-SE-directed extension and clockwise rotation. These sequential and variably oriented deformation episodes significantly influenced the geometry and kinematics of the East Sea opening. Overall, the southeastern Korean Peninsula records the integrated effects of subduction, continental rifting, and rotational oceanic opening, offering insights into the broader tectonic evolution around the East Asian margin.

CRediT authorship contribution statement

Seongjun Park: Writing – original draft, Methodology, Investigation, Conceptualization. **Tae-Kyung Hong:** Writing – review & editing, Writing – original draft, Supervision, Project administration, Funding acquisition, Conceptualization. **Jeongin Lee:** Validation, Investigation. **Junhyung Lee:** Visualization, Data curation. **Byeongwoo Kim:** Resources, Data curation.

Declaration of competing interest

The authors declare the following financial interests/personal relationships which may be considered as potential competing interests: Tae-Kyung Hong reports financial support was provided by National Research Foundation of Korea. If there are other authors, they declare that they have no known competing financial interests or personal relationships that could have appeared to influence the work reported in this paper.

Acknowledgments

We sincerely thank Dr. A. Vasanthi (editor) and two anonymous reviewers for their constructive comments, which improved the manuscript. The seismic waveforms were collected from the Korea Meteorological Administration (KMA) and Korea Institute of Geoscience and Mineral Resources (KIGAM). This work was supported by the Korea Meteorological Administration Research and Development Program under grant KMI2022-00710. Additionally, this research was partly supported by National Research Foundation of Korea (RS-2025-23963785).

Appendix A. Supplementary data

Supplementary material related to this article can be found online at https://doi.org/10.1016/j.gr.2026.08.023.

References

Bensen, G.D., Ritzwoller, M.H., Barmin, M.P., Levshin, A.L., Lin, F., Moschetti, M.P., Shapiro, N.M., Yang, Y., 2007. Processing seismic ambient noise data to obtain reliable broad-band surface wave dispersion measurements. Geophys. J. Int. 169, 1239–1260. http://dx.doi.org/10.1111/j.1365-246X.2007.03374.x.

Braeuer, B., Bauer, K., 2015. A new interpretation of seismic tomography in the southern Dead Sea basin using neural network clustering techniques. Geophys. Res. Lett. 42, 9772–9780. http://dx.doi.org/10.1002/2015GL066559.

Brocher, T.M., 2005. Empirical relations between elastic wavespeeds and density in the Earth's crust. Bull. Seismol. Soc. Am. 95, 2081–2092. http://dx.doi.org/10.1785/0120060403.

Celis, S., Hong, T.-K., Lee, J., Park, S., Liu, Y., Kim, B., Lee, J., Kim, D.G., 2025. Core-refracted shear-wave anisotropy beneath the Korean Peninsula: insights into its tectonic evolution. Gondwana Res. 148, 220–239. http://dx.doi.org/10.1016/j.gr.2025.07.018.

Chang, S.J., Baag, C.E., 2006. Crustal structure in southern Korea from joint analysis of regional broadband waveforms and travel times. Bull. Seismol. Soc. Am. 96, 856–870. http://dx.doi.org/10.1785/0120040165.

Cho, J.-D., Choi, J.-H., Lim, M.-T., Park, I.-H., Ko, I.-S., 1997. A Study on the Regional Gravity Anomaly (Southern Part of Korean Peninsula). KIGAM Research Report KR-96 (c)-5 (p. 27), Korea Institute of Geology and Mining and Materials., (in Korean).

Cho, K.H., Herrmann, R.B., Ammon, C.J., Lee, K., 2007. Imaging the upper crust of the Korean Peninsula by surface-wave tomography. Bull. Seismol. Soc. Am. 97, 198–207. http://dx.doi.org/10.1785/0120060096.

Cho, H., Lee, S.J., Kim, S., Rhie, J., Kang, T.S., 2025. Imaging the 3D basin structure of the Santa Clara Valley by ambient noise tomography. Geosci. J. 29, 87–101. http://dx.doi.org/10.1007/s12303-025-00005-8.

Choi, S., Choi, E.K., Kim, S.W., Lee, Y.C., 2021a. Expected segmentation of the chugaryung fault system estimated by the gravity field interpretation. Econ. Environ. Geol. 54, 743–752. http://dx.doi.org/10.9719/EEG.2021.54.6.743, (in Korean).

Choi, H., Hong, T.-K., He, X., Baag, C.E., 2012. Seismic evidence for reverse activation of a paleo-rifting system in the East Sea (sea of Japan). Tectonophysics 572, 123–133. http://dx.doi.org/10.1016/j.tecto.2011.12.023.

Choi, J., Kang, T.-S., Baag, C.-E., 2009. Three-dimensional surface wave tomography for the upper crustal velocity structure of southern Korea using seismic noise correlations. Geosci. J. 13, 423–432. http://dx.doi.org/10.1007/s12303-009-0040-2.

Choi, S., Kim, S.W., Choi, E.K., Lee, Y.C., Ha, S., 2021b. Gravity field interpretation and underground structure modelling as a method of setting horizontal and vertical zoning of a active fault core. Econ. Environ. Geol. 54, 91–103. http://dx.doi.org/10.14770/jgsk.2018.54.6.641, (in Korean).

Choi, S., Kim, S.W., Choi, E.K., Shin, Y., Hong, T.-K., 2022. Analysis of the causes of clustered scismicity registered in Yeoncheon, the middle part of the Korean peninsula through gravity field interpretation and modeling. Econ. Environ. Geol. 55, 633–648. http://dx.doi.org/10.9719/EEG.2022.55.6.633, (in Korean).

Chough, S.K., Kwon, S.-T., Ree, J.-H., Choi, D.K., 2000. Tectonic and sedimentary evolution of the Korean peninsula: a review and new view. Earth-Sci. Rev. 52, 175–235. http://dx.doi.org/10.1016/S0012-8252(00)00029-5.

Chough, S.K., Sohn, Y.K., 2010. Tectonic and sedimentary evolution of a cretaceous continental arc-backarc system in the Korean peninsula: New view. Earth-Sci. Rev. 101, 225–249. http://dx.doi.org/10.1016/j.earscirev.2010.05.004.

Du, M., Lei, J., Zhao, D., Lu, H., 2022. Pn anisotropic tomography of northeast Asia: New insight into subduction dynamics and volcanism. J. Geophys. Res.: Solid Earth 127, e2021. http://dx.doi.org/10.1029/2021JB023080, B023080.

Goutorbe, B., de Oliveira Coelho, D.L., Drouet, S., 2015. Rayleigh wave group velocities at periods of 6-23 s across Brazil from ambient noise tomography. Geophys. J. Int. 203, 869–882. http://dx.doi.org/10.1093/gji/ggv343.

Hafkenscheid, E., Wortel, M.J.R., Spakman, W., 2006. Subduction history of the tethyan region derived from seismic tomography and tectonic reconstructions. J. Geophys. Res.: Solid Earth 111, B08401. http://dx.doi.org/10.1029/2005JB003791.

Hao, S., Huang, Z., Han, C., Wang, L., Xu, M., Mi, N., Yu, D., 2021. Layered crustal azimuthal anisotropy beneath the northeastern Tibetan Plateau revealed by Rayleigh-wave Eikonal tomography. Earth Planet. Sci. Lett. 563, 116891. http://dx.doi.org/10.1016/j.epsl.2021.116891.

Hayashida, A., Fukui, T., Torii, M., 1991. Paleomagnetism of the early Miocene Kani group in southwest Japan and its implication for the opening of the Japan sea. Geophys. Res. Lett. 18, 1095–1098. http://dx.doi.org/10.1029/91GL01349.

Heo, D., Kang, T.-S., Kim, M., Ahn, B.S., Lim, H., Han, J., Kim, K.-H., Rhie, J., Kim, Y., Ree, J.H., 2024. New insights on seismic activity in the southeastern Korean peninsula from the Gyeongju Hi-density broadband seismic network (GHBSN). Geosci. J. 28, 319–333. http://dx.doi.org/10.1007/s12303-024-0003-7.

Herrmann, R.B., Ammon, C.J., 2004. Surface waves, receiver functions and crustal structure. In: Computer Programs in Seismology. Saint Louis University, version 3.30. Retrieved from http://www.eas.slu.edu/People/RBHerrmann/CPS330.html.

Hidayat, H., Nugraha, A.D., Priyono, A., Marjiyono, M., Setiawan, J.H., Sahara, D.P., Winardhi, S., Zulfakriza, Z., Rosalia, S., Lelonmo, E.B., Permana, A., Setiawan, A., 2021. Travel time tomography to delineate 3-D regional seismic velocity structure in the Banyumas Basin, Central Java, Indonesia, using dense borehole seismographic stations. Front. Earth Sci. 9, 639271. http://dx.doi.org/10.3389/feart.2021.639271.

Van van der Hilst, R.D., Widiyantoro, S., Engdahl, E.R., 1997. Evidence for deep mantle circulation from global tomography. Nature 386, 578–584. http://dx.doi.org/10.1038/386578a0.

Hirata, N., Karp, B.Y., Yamaguchi, T., Kanazawa, T., Suyehiro, K., Kasahara, J., Shiobara, H., Shinohara, M., Kinoshita, H., 1992. Oceanic crust in the Japan basin of the Japan sea by the 1990 Japan-USSR expedition. Geophys. Res. Lett. 19, 2027–2030. http://dx.doi.org/10.1029/92GL02094.

Hong, T.-K., 2010. Lg attenuation in a region with both continental and oceanic environments. Bull. Seismol. Soc. Am. 100, 851–858. http://dx.doi.org/10.1785/0120090057.

Hong, T.-K., Baag, C.E., Choi, H., Sheen, D.H., 2008. Regional seismic observations of the 9 october 2006 underground nuclear explosion in north Korea and the influence of crustal structure on regional phases. J. Geophys. Res.: Solid Earth 113, B03305. http://dx.doi.org/10.1029/2007JB004950.

Hong, T.-K., Choi, H., 2012. Seismological constraints on the collision belt between the north and south China blocks in the Yellow Sea. Tectonophysics 570, 102–113. http://dx.doi.org/10.1016/j.tecto.2012.08.034.

Hong, T.-K., Kang, T.S., 2009. Pn travel-time tomography of the paleo-continental-collision and rifting zone around Korea and Japan. Bull. Seismol. Soc. Am. 99, 416–421. http://dx.doi.org/10.1785/0120080120.

Hong, T.-K., Lee, K., 2012. Mb(Pn) scale for the Korean peninsula and site-dependent Pn amplification. Pure Appl. Geophys. 169, 1963–1975.

Hong, T.-K., Lee, J., Kim, W., Hahm, I.K., Woo, N.C., Park, S., 2017. The 12 September 2016 ML 5.8 midcrustal earthquake in the Korean Peninsula and its seismic implications. Geophys. Res. Lett. 44, 3131–3138. http://dx.doi.org/10.1002/2017GL072899.

Hong, T.-K., Lee, J., Kim, B., Park, S., Lee, J., Kim, D.G., Kang, T.S., 2025. Lower-crustal rupture of the 1952 M_w6.3 suburban Pyongyang earthquake: insights into seismogenic reactivation in a paleocollision zone and seismic hazard potential. Bull. Seismol. Soc. Am. 115, 2640–2656. http://dx.doi.org/10.1785/0120250104.

Hong, T.-K., Lee, J., Lee, G., Lee, J., Park, S., 2020. Correlation between ambient seismic noises and economic growth. Seismol. Res. Lett. 91, 2343–2354. http://dx.doi.org/10.1785/0220190369.

Hong, T.-K., Lee, J., Park, S., Kim, W., 2018. Time-advanced occurrence of moderate-size earthquakes in a stable intraplate region after a megathrust earthquake and their seismic properties. Sci. Rep. 8, 13331. http://dx.doi.org/10.1038/s41598-018-31600-5.

Hong, T.-K., Lee, J., Park, S., Kim, W., 2022. Major influencing factors for the nucleation of the 15 November 2017 M_W5.5 Pohang earthquake. Phys. Earth Planet. Inter. 323, 106833. http://dx.doi.org/10.1016/j.pepi.2021.106833.

Hong, T.-K., Park, S., Houng, S.E., 2016. Seismotectonic properties and zonation of the far-eastern eurasian plate around the Korean Peninsula. Pure Appl. Geophys. 173, 1175–1195. http://dx.doi.org/10.1007/s00024-015-1170-2.

Hong, T.-K., Park, S., Lee, J., Lee, J., Kim, B., 2024. Middle to lower crustal earthquakes in the western east sea (sea of japan) and their implications for neotectonic evolution. Tectonophysics 230346. http://dx.doi.org/10.1016/j.tecto.2024.230346.

Huang, J., Zhao, D., 2006. High-resolution mantle tomography of China and surrounding regions. J. Geophys. Res.: Solid Earth 111, 09305. http://dx.doi.org/10.1029/2005JB004066.

Hwang, J.Y., Chang, S.J., 2023. Analysis of crustal velocity structure beneath gangwon province, South Korea, using joint inversion of receiver functions and surface wave dispersion. Econ. Environ. Geol. 56, 277–291. http://dx.doi.org/10.9719/EEG.2023.56.3.277, (in Korean).

Jia, Z., Clayton, R.W., 2021. Determination of near surface shear-wave velocities in the central Los Angeles basin with dense arrays. J. Geophys. Res.: Solid Earth 126, e2020. http://dx.doi.org/10.1029/2020JB021369, B021369.

Jin, G., Gaherty, J.B., 2015. Surface wave phase-velocity tomography based on multichannel cross-correlation. Geophys. J. Int. 201, 1383–1398. http://dx.doi.org/10.1093/gji/ggv079.

Jo, E., Hong, T.-K., 2013. V_P/V_S ratios in the upper crust of the southern Korean Peninsula and their correlations with seismic and geophysical properties. J. Asian Earth Sci. 66, 204–214. http://dx.doi.org/10.1016/j.jseaes.2013.01.008.

Jolivet, L., Tamaki, K., Fournier, M., 1994. Japan sea, opening history and mechanism: A synthesis. J. Geophys. Res.: Solid Earth 99, 22237–22259. http://dx.doi.org/10.1029/93JB03463.

Kang, D., Shen, W., Ning, J., Ritzwoller, M.H., 2016. Seismic evidence for lithospheric modification associated with intracontinental volcanism in Northeastern China. Geophys. J. Int. 204, 215–235. http://dx.doi.org/10.1093/gji/ggv441.

Kennett, B.L., Engdahl, E.R., Buland, R., 1995. Constraints on seismic velocities in the Earth from traveltimes. Geophys. J. Int. 122, 108–124. http://dx.doi.org/10.1111/j.1365-246X.1995.tb03540.x.

Kil, D., Hong, T.-K., Chung, D., Kim, B., Lee, J., Park, S., 2021. Ambient noise tomography of upper crustal structures and quaternary faults in the seoul metropolitan area and its geological implications. Earth Space Sci. 8, e2021. http://dx.doi.org/10.1029/2021EA001983, A001983.

Kim, B., Hong, T.-K., 2022. A national V_{S30} model for South Korea to combine nationwide dense borehole measurements with ambient seismic noise analysis. Earth Space Sci. 9, e2021. http://dx.doi.org/10.1029/2021EA002066, A002066.

Kim, H.-J., Jou, H.-T., Lee, G.H., 2018. Neotectonics of the eastern Korean margin inferred from back-arc rifting structure. Ocean. Sci. J. 53, 601–609. http://dx.doi.org/10.1007/s12601-018-0036-9.

Kim, S.W., Kwon, S., Ryu, I.-C., Jeong, Y.-J., Choi, S.-J., Kee, W.-S., Yi, K., Lee, Y.S., Kim, B.C., Park, D.W., 2012. Characteristics of the early cretaceous igneous activity in the Korean Peninsula and tectonic implications. J. Geol. 120, 625–646. http://dx.doi.org/10.1086/667811.

Kim, H.-J., Lee, G.H., Jou, H.T., Cho, H.M., Yoo, H.S., Park, G.T., Kim, J.S., 2007. Evolution of the eastern margin of Korea: Constraints on the opening of the East Sea (Japan sea). Tectonophysics 436, 37–55. http://dx.doi.org/10.1016/j.tecto.2007.02.014.

Kim, Y., Lee, C., Kim, S.S., 2015. Tectonics and volcanism in east Asia: Insights from geophysical observations. J. Asian Earth Sci. 113, 842–856. http://dx.doi.org/10.1016/j.jseaes.2015.07.032.

Kim, H., Lee, H., Song, J.H., Lee, W., Hong, J., Kagoshima, T., Takahata, N., Sano, Y., Fischer, T.P., 2024. Latent magmatism beneath the Korean Peninsula caused by asthenosphere upwelling. Commun. Earth Environ. 5, 427. http://dx.doi.org/10.1038/s43247-024-01592-4.

Kim, H.-J., Moon, S., Kim, C., Kim, K.-H., Seo, W., Cho, K.-H., Moon, H.-J., Lee, G.H., 2022. Neotectonics at the SE continental margin of the Korean peninsula: Implications for the back-arc region behind the SW Japan arc. Pure Appl. Geophys. 179, 3945–3966. http://dx.doi.org/10.1007/s00024-022-02979-0.

Kim, K.H., Park, J.H., Park, Y., Hao, T.Y., Kim, H.J., 2017. Crustal structure beneath the southern Korean Peninsula from local earthquakes. Geophys. J. Int. 209, 969–978. http://dx.doi.org/10.1093/gji/ggx079.

Kim, S., Rhie, J., Kim, G., 2011. Forward waveform modelling procedure for 1-D crustal velocity structure and its application to the southern Korean Peninsula. Geophys. J. Int. 185, 453–468. http://dx.doi.org/10.1111/j.1365-246X.2011.04949.x.

King, S.D., Anderson, D.L., 1998. Edge-driven convection. Earth Planet. Sci. Lett. 160, 289–296. http://dx.doi.org/10.1016/S0012-821X(98)00089-2.

Lee, S., Choi, E., Son, M., Song, S.G., Gómez, D.D., 2025. Viscoelastic modelling reveals correlation between GNSS-derived deformation rates after the 2011 Tohoku-Oki earthquake and lithospheric thickness in the southern Korean Peninsula. Geophys. J. Int. 242, ggaf182. http://dx.doi.org/10.1093/gji/ggaf182.

Lee, J., Hong, T.-K., Chang, C., 2017. Crustal stress field perturbations in the continental margin around the Korean Peninsula and Japanese islands. Tectonophysics 718, 140–149. http://dx.doi.org/10.1016/j.tecto.2017.08.003.

Lee, J., Hong, T.-K., Park, S., Kim, B., Celis, S., Liu, Y., 2025. Continent-side paleo-rift structure in the western East Sea (sea of Japan) and linkage between Moho uplift and mountain range formation. J. Geophys. Res.: Solid Earth 130, e2025. http://dx.doi.org/10.1029/2025JB031780, B031780.

Lee, Y.I., Lee, J.I., Choi, Y.S., 2023. Provenance analysis of the cretaceous Gyeongsang Basin, SE Korea: A synthesis and tectonic implications for active continental margin in East Asia. Earth-Sci. Rev. 238, 104334. http://dx.doi.org/10.1016/j.earscirev.2023.104334.

Lee, S.H., Oh, C.W., Cho, D.-L., Lee, B.C., Lee, B.Y., 2023. Early cretaceous magmatism in the northern Gyeonggi Massif and the northcentral Yeongnam Massif, Korean Peninsula: Its implications for the cretaceous tectonic evolution of the Northeast Asia. Lithos 460, 107366. http://dx.doi.org/10.1016/j.lithos.2023.107366.

Lee, Y., Park, S., Kim, J., Kim, H.C., Koo, M.H., 2010. Geothermal resource assessment in Korea. Renew. Sustain. Energy Rev. 14, 2392–2400. http://dx.doi.org/10.1016/j.rser.2010.05.003.

Lee, S., Saxena, A., Song, J.H., Rhie, J., Choi, E., 2022. Contributions from lithospheric and upper-mantle heterogeneities to upper crustal seismicity in the Korean Peninsula. Geophys. J. Int. 229, 1175–1192. http://dx.doi.org/10.1093/gji/ggab527.

Lee, S., Song, J.H., Heo, D., Rhie, J., Kang, T.S., Choi, E., Kim, Y., Kim, K.-H., Ree, J.H., 2023. Crustal and uppermost mantle structures imaged by teleseismic P-wave traveltime tomography beneath the southeastern Korean Peninsula: implications for a hydrothermal system controlled by the thermally modified lithosphere. Geophys. J. Int. 235, 1639–1657. http://dx.doi.org/10.1093/gji/ggad319.

Lehujeur, M., Chevrot, S., 2020. On the validity of the eikonal equation for surface-wave phase-velocity tomography. Geophys. J. Int. 223, 908–914. http://dx.doi.org/10.1093/gji/ggaa352.

Lei, J., Zhao, D., 2005. P-wave tomography and origin of the Changbai intraplate volcano in Northeast Asia. Tectonophysics 397, 281–295. http://dx.doi.org/10.1016/j.tecto.2004.12.009.

Levshin, A.L., Yanovskaya, T.B., Lander, A.V., Bukchin, B.G., Barmin, M.P., Ratnikova, L.I., Its, E.N., 1989. In: Keilis-Borok, V.I. (Ed.), Seismic surface waves in a laterally inhomogeneous Earth. Kluwer, http://dx.doi.org/10.1007/978-94-009-0883-3.

Li, Y., Wu, Q., Pan, J., Zhang, F., Yu, D., 2013. An upper-mantle S-wave velocity model for east Asia from Rayleigh wave tomography. Earth Planet. Sci. Lett. 377, 367–377. http://dx.doi.org/10.1016/j.epsl.2013.06.033.

Lin, F.C., Li, D., Clayton, R.W., Hollis, D., 2013. High-resolution 3D shallow crustal structure in Long Beach, California: Application of ambient noise tomography on a dense seismic array. Geophysics 78, Q45–Q56. http://dx.doi.org/10.1190/geo2012-0453.1.

Lin, F.C., Ritzwoller, M.H., 2011a. Apparent anisotropy in inhomogeneous isotropic media. Geophys. J. Int. 186, 1205–1219.

Lin, F.C., Ritzwoller, M.H., 2011b. Helmholtz surface wave tomography for isotropic and azimuthally anisotropic structure. Geophys. J. Int. 186, 1104–1120. http://dx.doi.org/10.1111/j.1365-246X.2011.05070.x.

Liu, Y., Hong, T.-K., Lee, J., Park, S., Celis, S., Chen, Y., Lee, J., Kim, B., 2026. Tomographic constraints on the collision boundary between the Yangtze Block and the Sino-Korean craton and Yellow Sea Basin extension. Gondwana Res. 151, 390–408. http://dx.doi.org/10.1016/j.gr.2025.11.006.

Long, M.D., van der Hilst, R.D., 2005. Upper mantle anisotropy beneath Japan from shear wave splitting. Phys. Earth Planet. Inter. 151, 206–222. http://dx.doi.org/10.1016/j.pepi.2005.03.003.

Lü, Y., Li, J., Liu, L., Zhao, L.F., 2019. Complex uppermost mantle structure and deformation beneath the Northwest Pacific region. J. Geophys. Res.: Solid Earth 124, 6866–6879. http://dx.doi.org/10.1029/2019JB017356.

Ma, Q., Xu, Y.G., 2021. Magmatic perspective on subduction of paleo-Pacific plate and initiation of big mantle wedge in east Asia. Earth-Sci. Rev. 213, 103473. http://dx.doi.org/10.1016/j.earscirev.2020.103473.

Martin, A.K., 2011. Double saloon door tectonics in the Japan sea, Fossa magna, and the Japanese island arc. Tectonophysics 498, 45–65. http://dx.doi.org/10.1016/j.tecto.2010.11.016.

Nafe, J.E., Drake, C.L., 1963. Physical properties of marine sediments. In: Hill, M.N. (Ed.), In: The Sea, vol. 3, Interscience, pp. 794–815.

Nakajima, J., Shimizu, J., Hori, S., Hasegawa, A., 2006. Shear-wave splitting beneath the southwestern Kurile arc and northeastern Japan arc: A new insight into mantle return flow. Geophys. Res. Lett. 33, http://dx.doi.org/10.1029/2005GL025053.

Okada, H., 2000. Nature and development of cretaceous sedimentary basins in east Asia: a review. Geosci. J. 4, 271–282. http://dx.doi.org/10.1007/BF02914036.

Otofuji, Y.I., Enami, R., Yokoyama, M., Kamiya, K., Kuma, S., Saito, H., Matsuda, T., 1999. Miocene clockwise rotation of southwest Japan and formation of curvature of the median tectonic line: Paleomagnetic implications. J. Geophys. Res.: Solid Earth 104, 12895–12907. http://dx.doi.org/10.1029/1999JB900086.

Otofuji, Y.I., Matsuda, T., Nohda, S., 1985. Paleomagnetic evidence for the miocene counter-clockwise rotation of northeast Japan-rifting process of the Japan arc. Earth Planet. Sci. Lett. 75, 265–277. http://dx.doi.org/10.1016/0012-821X(85)90108-6.

Park, S., Chang, S.J., Lee, J., Chung, D., Kim, B., Park, S., Hong, T.-K., 2024. Crustal and uppermost mantle S-velocity structure of the Seoul metropolitan area on the Korean Peninsula from Helmholtz tomography. Tectonophysics 891, 230518. http://dx.doi.org/10.1016/j.tecto.2024.230518.

Park, S., Hong, T.-K., 2020. Typhoon-induced microseisms around the south China sea. Seism. Soc. Am. 91, 3454–3468. http://dx.doi.org/10.1785/0220190310.

Park, S., Hong, T.-K., 2024a. Continent-side uplifted mantle and geological imprints along a paleo rift in the western East Sea (Sea of Japan). J. Geophys. Res.: Solid Earth 129, e2024. http://dx.doi.org/10.1029/2024JB029049, B029049.

Park, S., Hong, T.-K., 2024b. Correct off-site determination of seismic sensor orientation from combined analyses of earthquake and microseism records. Bull. Seismol. Soc. Am. 114, 942–954. http://dx.doi.org/10.1785/0120230150.

Park, S., Hong, T.-K., 2026. Microseisms as a renewable energy resource: Nature of ubiquitous, unrelenting, and coherent ground vibrations and energy flow. Renew. Energy 123894. http://dx.doi.org/10.1016/j.renene.2025.123894.

Park, S., Hong, T.-K., Lee, J., 2022. Determination of borehole seismic sensor orientation using microseisms. Bull. Seismol. Soc. Am. 112, 2327–2343. http://dx.doi.org/10.1785/0120220002.

Park, S., Hong, T.-K., Rah, G., 2021. Seismic hazard assessment for the Korean peninsula. Bull. Seismol. Soc. Am. 111, 2696–2719. http://dx.doi.org/10.1785/0120200261.

Pasyanos, M.E., Masters, T.G., Laske, G., Ma, Z., 2014. LITHO1.0: An updated crust and lithospheric model of the earth. J. Geophys. Res.: Solid Earth 119, 2153–2173. http://dx.doi.org/10.1002/2013JB010626.

Rawlinson, N., Sambridge, M., 2003. Seismic traveltime tomography of the crust and lithosphere. Adv. Geophys. 46, 81–199. http://dx.doi.org/10.1016/s0065-2687(03)46002-0.

Replumaz, A., Negredo, A.M., Guillot, S., Villaseñor, A., 2010. Multiple episodes of continental subduction during India/Asia convergence: Insight from seismic tomography and tectonic reconstruction. Tectonophysics 483, 125–134. http://dx.doi.org/10.1016/j.tecto.2009.10.007.

Ryu, I.C., Choi, S.G., Wee, S.M., 2006. An inquiry into the formation and deformation of the cretaceous Gyeongsang (Kyongsang) Basin, Southeastern Korea. Econ. Environ. Geol. 39, 129–149, (in Korean).

Shapiro, N.M., Campillo, M., 2004. Emergence of broadband Rayleigh waves from correlations of the ambient seismic noise. Geophys. Res. Lett. 31, L07614. http://dx.doi.org/10.1029/2004GL019491.

Shapiro, N.M., Campillo, M., Stehly, L., Ritzwoller, M.H., 2005. High-resolution surface-wave tomography from ambient seismic noise. Science 307, 1615–1618. http://dx.doi.org/10.1126/science.1108339.

Song, J.H., Kim, S., Rhie, J., 2020. Heterogeneous modification and reactivation of a craton margin beneath the Korean Peninsula from teleseismic travel time tomography. Gondwana Res. 81, 475–489. http://dx.doi.org/10.1016/j.gr.2019.11.016.

Sun, Y., Liu, M., 2023. Edge-driven asthenospheric convection beneath the north China craton: A numerical study. Tectonophysics 849, 229726. http://dx.doi.org/10.1016/j.tecto.2023.229726.

Syracuse, E.M., van Keken, P.E., Abers, G.A., 2010. The global range of subduction zone thermal models. Phys. Earth Planet. Inter. 183, 73–90. http://dx.doi.org/10.1016/j.pepi.2010.02.004.

Tang, J., Xu, W., Wang, F., Ge, W., 2018. Subduction history of the paleo-Pacific slab beneath eurasian continent: Mesozoic-paleogene magmatic records in northeast Asia. Sci. China Earth Sci. 61, 527–559. http://dx.doi.org/10.1007/s11430-017-9174-1.

Yang, Y., Ritzwoller, M.H., Levshin, A.L., Shapiro, N.M., 2007. Ambient noise Rayleigh wave tomography across Europe. Geophys. J. Int. 168, 259–274. http://dx.doi.org/10.1111/j.1365-246X.2006.03203.x.

Yang, G., Zhao, L.F., Xie, X.B., He, X., Lü, Y., Yao, Z.X., 2022. Double door, opening of the Japan sea inferred by Pn attenuation tomography. Geophys. Res. Lett. 49, e2022. http://dx.doi.org/10.1029/2022GL099886, L099886.

Zhao, D., Maruyama, S., Omori, S., 2007. Mantle dynamics of western Pacific and east Asia: Insight from seismic tomography and mineral physics. Gondwana Res. 11, 120–131. http://dx.doi.org/10.1016/j.gr.2006.06.006.

Zhao, D., Tian, Y., Lei, J., Liu, L., Zheng, S., 2009. Seismic image and origin of the Changbai intraplate volcano in east Asia: Role of big mantle wedge above the stagnant Pacific slab. Phys. Earth Planet. Inter. 173, 197–206. http://dx.doi.org/10.1016/j.pepi.2008.11.009.

Zhao, D., Yanada, T., Hasegawa, A., Umino, N., Wei, W., 2012. Imaging the subducting slabs and mantle upwelling under the Japan islands. Geophys. J. Int. 190, 816–828. http://dx.doi.org/10.1111/j.1365-246X.2012.05550.x.